AD-A062 492 BATTELLE COLUMBUS LABS OHIO F/G 20/4
WATER-DROPLET IMPACT-CHARACTERIZATION OF DAMAGE MECHANISMS.(U)
NOV 78 R G HOAGLAND, R G JUNG N00014-76-C-0645
UNCLASSIFIED NL

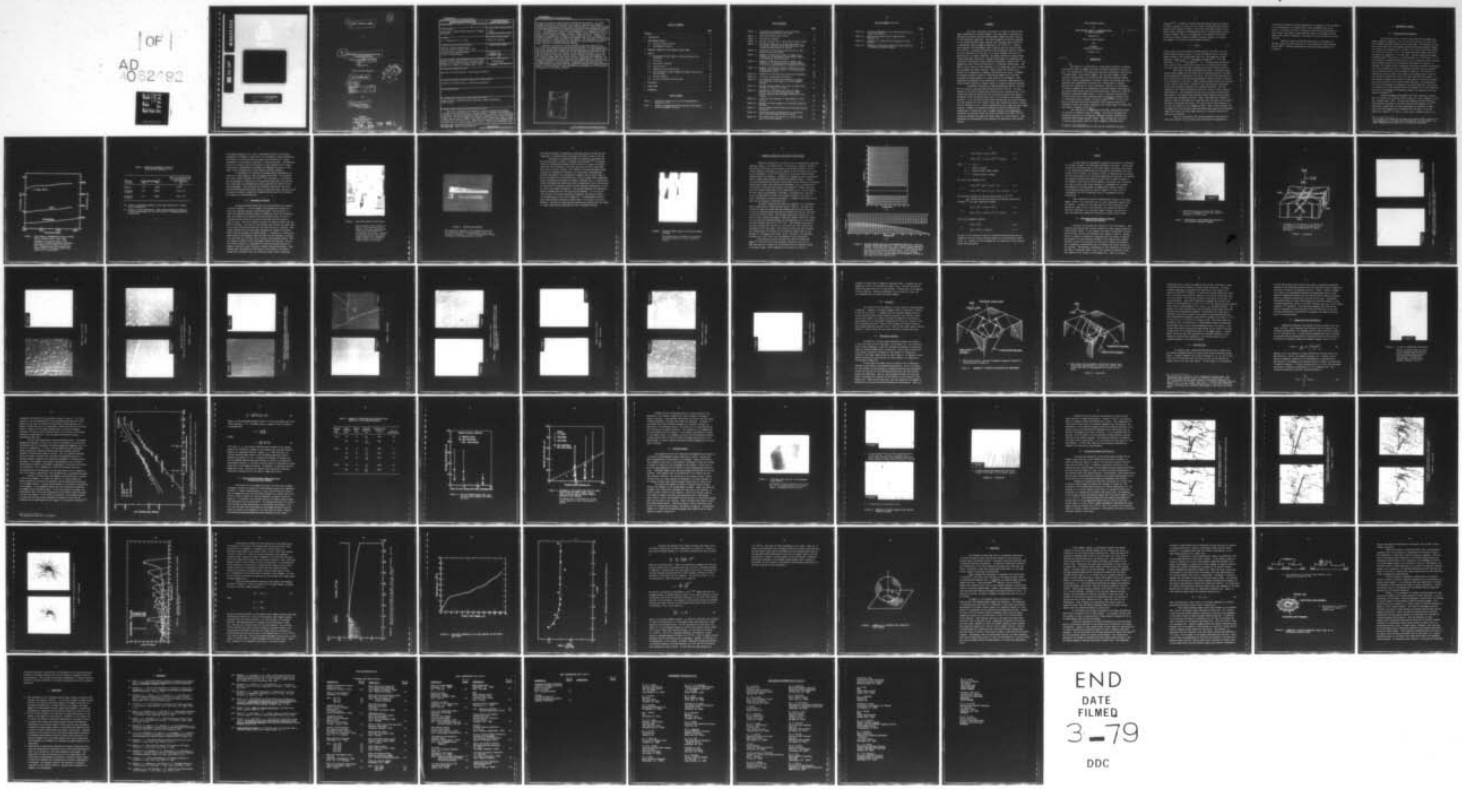

END
DATE FILMED
3-79
DDC

AD A062492

DDC FILE COPY

This document has been approved for public release and sale; its distribution is unlimited.

(9) FINAL TECHNICAL REPORT,

(12)

on

(6) WATER-DROPLET IMPACT-CHARACTERIZATION OF DAMAGE MECHANISMS,

Contract No. N000(14)-76-C-0645
(15)

prepared for

Office of Naval Research

(11) November 1978

(12) 78p.

This document has been approved for public release and sale; its distribution is unlimited.

DDC
DEC 26 1978
F

by

(10) R. G./Hoagland
and R. G./Jung

BATTELLE
Columbus Laboratories
505 King Avenue
Columbus, Ohio 43201

78 12 20 021
489080
LB

UNCLASSIFIED

SECURITY CLASSIFICATION OF THIS PAGE (When Data Entered)

REPORT DOCUMENTATION PAGE		READ INSTRUCTIONS BEFORE COMPLETING FORM
1. REPORT NUMBER	2. GOVT ACCESSION NO.	3. RECIPIENT'S CATALOG NUMBER
4. TITLE (and Subtitle) Water-Droplet Impact-Characterization of Damage Mechanisms		5. TYPE OF REPORT & PERIOD COVERED Final 6. PERFORMING ORG. REPORT NUMBER
7. AUTHOR(s) R. G. Hoagland and R. G. Jung		8. CONTRACT OR GRANT NUMBER(s) N00014-76-C-0645
9. PERFORMING ORGANIZATION NAME AND ADDRESS Battelle, Columbus Laboratories 505 King Avenue, Columbus, Ohio 43201		10. PROGRAM ELEMENT, PROJECT, TASK AREA & WORK UNIT NUMBERS
11. CONTROLLING OFFICE NAME AND ADDRESS Office of Naval Research		12. REPORT DATE November 1978 13. NUMBER OF PAGES 63
14. MONITORING AGENCY NAME & ADDRESS (if different from Controlling Office) Defense Contract Administration, Services Office, Columbus, c/o Defense Construction Supply Center, Building #1, Section #1, Columbus, Ohio 43215		15. SECURITY CLASS. (of this report) UNCLASSIFIED 15a. DECLASSIFICATION/DOWNGRADING SCHEDULE

16. DISTRIBUTION STATEMENT (of this Report)

Approved for Public Release. Distribution Unlimited.

17. DISTRIBUTION STATEMENT (of the abstract entered in Block 20, if different from Report)

Approved for Public Release. Distribution Unlimited.

18. SUPPLEMENTARY NOTES

19. KEY WORDS (Continue on reverse side if necessary and identify by block number)

Impact Erosion, Lithium Fluoride, Cratering, Computer Simulation, Etch Pitting

20. ABSTRACT (Continue on reverse side if necessary and identify by block number)

This report describes the results of a series of water-droplet-impact experiments on lithium fluoride. The work seeks to determine the deformation processes occurring during droplet impact and their relation to bulk mechanical properties. The flow strengths and fracture toughness of the lithium fluoride single crystals used as targets were varied over a considerable range by gamma irradiation to 10^6 R and 10^7 R. Impacts were produced by 0.4-mm-diameter water droplets over the velocity range 60 to 160 m/s. Dislocations involved in the

DD FORM 1 JAN 73 1473 EDITION OF 1 NOV 65 IS OBSOLETE

UNCLASSIFIED

SECURITY CLASSIFICATION OF THIS PAGE (When Data Entered)

deformation induced by impacting were revealed by etch pitting. At a given strength level and for a particular set of impact conditions, the damage produced by single-droplet impacts shows wide variability, ranging from movement of preexisting dislocations to dislocation rosette patterns containing a central crater. The damage-zone sizes conform statistically to a log-normal distribution. The median values indicate a weak dependence of the damage-zone sizes on stress, bulk strength, and impact velocity. These results are believed to be related to the generation of damage in dislocation-free areas. Estimates of stresses required to punch in dislocations suggest that very high pressures are being produced in a small fraction of the impacts. This hypothesis is supported by the observation of apparently small amounts of molten material adjacent to impact craters on a multiply impacted specimen.

A numerical calculation in finite-difference form was conducted for a 0.4 mm dia. drop impacting lithium fluoride at 100 m/s. The model employed a very finely divided mesh network and time increments with a view towards exploring the possibility that refining the spatial and temporal increments in the calculation would lead to an increase in the predicted pressures. Up to the time the shock wave detached from the contact boundary the peak pressure was only slightly larger than predicted by earlier calculations of Rosenblatt, et. al. and was approximately three times the water hammer pressure. However, the pressures developed in these calculations are insufficient to produce the type of damage observed in the experiments. Mechanisms are discussed which may provide pressures much higher than the numerical estimates for spherical droplet impact on a solid surface. These mechanisms rely principally on the existance of asperities on the droplet surface.

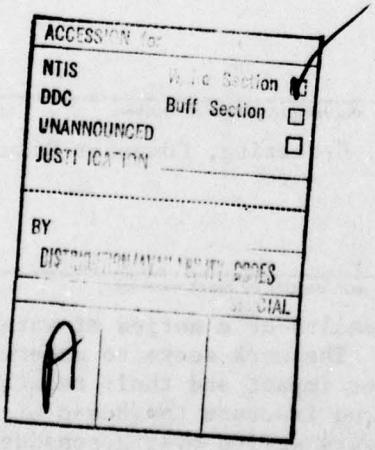

TABLE OF CONTENTS

	Page
ABSTRACT	iv
1. INTRODUCTION	1
2. EXPERIMENTAL DETAILS	4
2.1. Material Characterization	4
2.2. Impingement Procedure	7
3. NUMERICAL MODELING OF THE DROPLET IMPACT EVENT	12
4. RESULTS	15
4.1. Discrepancy Between Number of Impacts Observed and Predicted	15
4.2. Cratering	27
4.3. Dislocation Punching	27
4.4. Nonlocal Slip	30
4.5. Damage-Zone Size Distribution	31
4.6. Relation Between Impact Damage and Impact Velocity and Flow Strength	35
4.7. Multiple Impacts	39
4.8. Calculated Pressure Distributions	43
5. DISCUSSION	56
6. CONCLUSIONS	61
7. REFERENCES	62

LIST OF TABLES

Table 1.	Mechanical Properties of the LiF Single-Crystal Material at 25 C	6
Table 2.	Summary of Damage-Zone Sizes Resulting from Impacts by 0.4-mm-Diameter Droplets	36

LIST OF FIGURES

		Page
Figure 1.	Flow Curves in Compression of the LiF Single-Crystal Materials Used in this Study	5
Figure 2.	High Speed Droplet Impact Device	8
Figure 3.	Rotating Arm Assembly	9
Figure 4.	Droplets Forming from an Oscillating Stream of Water .	11
Figure 5.	Mesh Network Employed in the Numerical Model of a 0.4 mm Dia. Sperhical Water Drop Impacting a Flat Lithium Fluoride Surface at 100 m/s	13
Figure 6.	Orientation of Slip Planes and Direction of Slip Caused by Hertzian Stresses	16
Figure 7.	Examples of Dislocation Arrays in Damage Zones Produced by 0.4-mm Diameter Water-Droplet Impacts on Unirradiated Lithium Fluoride	18
Figure 8.	Examples of Dislocation Arrays in Damage Zones Produced by 0.4-mm-Diameter Water Droplet Impacts at 96 m/s on Lithium Fluoride γ-Irradiated to 10^6 R .	21
Figure 9.	Examples of Dislocation Arrays Produced by 0.4-mm Diameter Water-Droplet Impacts on Lithium Fluoride γ-Irradiated to 10^7 R	23
Figure 10.	Schematics of Probable Dislocation-Loop Arrangement .	28
Figure 11.	A Field of Preexisting Dislocations	32
Figure 12.	The Log-Normal Cumulative Probability of Damage-Zone Sizes for 96 m/s Impact of 0.4-mm Diameter Droplets	34
Figure 13.	Relation Between Damage Zones Sizes and Bulk Yield Strength for Impacts at 96 m/s	37
Figure 14.	Dependence of the Damage Zone Sizes on Impact Velocity for the Three Strength Levels (CRSS, Critical Resolved Shear Strength) Employed in this Program	38
Figure 15.	A Specimen After Exposure to Approximately 18,000 Impacts	40
Figure 16.	Examples of Surface Damage on the Multiply Impacted Specimen	41
Figure 17.	Surface Damage Features Revealed by Scanning Electron Microscopy	44
Figure 18.	Calculated Pressure Distributions on the Contact Area at Selected Times During the Impact	48
Figure 19.	The Particle Velocity Pattern in the Drop 2.2394 nsec. After First Contact	50

LIST OF FIGURES (Continued)

		Page
Figure 20.	Calculated Dependence of the Peak Pressure on the Contact Area Radius	51
Figure 21.	Hypothetical Sound Velocity Computed From Equation (6)	52
Figure 22.	Schematic of a Sperhical Drop Impacting a Solid Surface	55
Figure 23.	Schematics of Multiply Connected Contact Areas Due to Nonspherical Droplet Shapes	59

ABSTRACT

This report describes the results of a series of water-droplet-impact experiments on lithium fluoride. The work seeks to determine the deformation processes occurring during droplet impact and their relation to bulk mechanical properties. The flow strengths and fracture toughness of the lithium fluoride single crystals used as targets were varied over a considerable range by gamma irradiation to 10^6 R and 10^7 R. Impacts were produced by 0.4-mm-diameter water droplets over the velocity range 60 to 160 m/s. Dislocations involved in the deformation induced by impacting were revealed by etch pitting. At a given strength level and for a particular set of impact conditions, the damage produced by single-droplet impacts shows wide variability, ranging from movement of preexisting dislocations to dislocation rosette patterns containing a central crater. The damage-zone sizes conform statistically to a log-normal distribution. The median values indicate a weak dependence of the damage-zone sizes on stress, bulk strength, and impact velocity. These results are believed to be related to the generation of damage in dislocation-free areas. Estimates of stresses required to punch in dislocations suggest that very high pressures are being produced in a small fraction of the impacts. This hypothesis is supported by the observation of apparently small amounts of molten material adjacent to impact craters on a multiply impacted specimen.

A numerical calculation in finite-difference form was conducted for a 0.4 mm dia. drop impacting lithium fluoride at 100 m/s. The model employed a very finely divided mesh network and time increments with a view towards exploring the possibility that refining the spatial and temporal increments in the calculation would lead to an increase in the predicted pressures. Up to the time the shock wave detached from the contact boundary the peak pressure was only slightly larger than predicted by earlier calculations of Rosenblatt, et al. and was approximately three times the water hammer pressure. However, the pressures developed in these calculations are insufficient to produce the type of damage observed in the experiments. Mechanisms are discussed which may provide pressures much higher than the numerical estimates for spherical droplet impact on a solid surface. These mechanisms rely principally on the existence of asperities on the droplet surface.

FINAL TECHNICAL REPORT

on

WATER-DROPLET IMPACT -- CHARACTERIZATION OF DAMAGE MECHANISMS

prepared for

Office of Naval Research

from

BATTELLE
Columbus Laboratories

November 1978

1. INTRODUCTION

The impact of a water drop on a solid surface produces a transient stress pulse which can damage the surface by plastic deformation and cracking. The consequence of this damage has important technological implications in diverse areas. Water droplet damage, like cavitation damage, is most typically characterized as an erosion process reflecting material removed with time. Indeed, measurements of material removal rates during repetitive impacting under standardized conditions are a common means of ranking materials for comparison of erosion resistance. However, the development of surface roughness (due to deformation or material removal) and damage in the surface layer during repetitive impacting greatly complicates a detailed analysis of individual impact events. In fact, qualitative descriptions of erosion show that several mechanisms may be involved at different times in the erosion process, leading to distinct stages.[1,2]* It is also clear that the conditions which will eventually lead to material removal are developed by sonic and subsonic droplets in the initial stage of erosion when the density of impacts is low.

The conditions of an impact are more easily characterized during the initial or incubation stage of erosion. The surface topography and mechanical properties of the impacted solid may be better established or controlled before damage becomes intense. This advantage has been used in several experimental studies of impact damage by individual water

*A table of references indicated in the text are contained in Section 7.

droplets.[3,4] In addition, results obtained through numerical modeling of droplet impacts are likely to be in better correspondence with experimental events because the ideally flat surface typically assumed in such models better simulates a microscopically flat or polished surface devoid of impact damage. Even so, the magnitude of the pressure distribution predicted by several numerical models of droplet impacts do not agree. For example, if we modify the water-hammer pressure to

$$P = \beta \rho_o C_o V , \tag{1}$$

where ρ_o and C_o are the density and sound speed of the fluid, V is the relative impact velocity, and $\beta = 1$ gives the familar form of the water-hammer pressure, then the following values of β are predicted at peak pressures: Huang, et al.[5], 0.68; Hwang and Hammitt[6], $\sim$ 1.0; and Rosenblatt, et al.[7,8] and Heymann[9], 2.7. An interesting observation with regard to these predictions is that the calculations which employ the more refined mesh and time increments also predict larger pressures.

This report describes experiments that seek to correlate single droplet impact damage with the nature of the loading produced by the impact and the mechanical properties of the solid. One of the principal goals of this research was to identify the mechanisms of erosion and their relations to the strengths of the solid. Single-crystal lithium fluoride was selected as the target in this study. Details of the flow patterns around impact surface were revealed by chemical etch pitting techniques. The flow strength of the lithium fluoride was varied by a factor of about eight by gamma radiation. The irradiation process does not alter the dislocation substructure. The impacts were produced by water droplets with precisely controlled size and impact velocity. Impact velocities were confined to subsonic levels of 160 meters per second and less, with most of the results obtained at 100 meters per second. The results show a wide variation in the size and character of the damage patterns. There is also evidence that the magnitude of the pressures generated during some impacts is considerably higher than either the water hammer pressure or pressures predicted by numerical calculations.

There is the prospect that previous numerical calculations of water drop impacts on flat surfaces have understated the magnitude of

the pressure distribution which developed as a consequence of the coarseness of the distribution of the mesh sizes or time increments used in the models. To explore this point a numerical calculation was performed for a water droplet impacting a lithium fluoride surface using highly refined spacial and temporal increments. The results of this calculation are also reported.

Finally, several interesting observations are presented for multiple impacts and these also point to the existance of high pressures during impact. Possible mechanisms for generating high pressures are discussed.

2. EXPERIMENTAL DETAILS

2.1. Material Characterization

The LiF single crystals used in this study were purchased from Harshaw Chemical Company as 1 cm x 1/2 cm x 10-cm bars, all of which had been cleaved along {100} planes from the same ingot. The crystals had less than 50 ppm impurities with magnesium being the principal impurity element. The crystals were annealed in air at 600 C for 12 hours and furnace cooled over an 84-hour period to 30 C. The final dislocation density produced by the anneal was typically 1×10^5 disl./cm^2. Several crystals were gamma irradiated from a ^{60}Co source to total exposures of 1×10^6 R and 1×10^7 R. The irradiation introduces point defects (e.g., interstitial fluorine atoms) which strongly interact with dislocations and harden the crystals. To determine the strength levels, compression tests were conducted on specimens from the as-annealed and the two irradiated conditions and the resulting true stress-true strain curves are shown in Figure 1. The direction of loading was along the [001], and therefore, the maximum shear stress was most favorably oriented for slip on the (011) and (101) slip planes*. In the annealed condition the crystals are quite soft, as the yield strength (0.2 percent strain) is only about 6.2 MPa (900 psi). On irradiating to 10^6 R the yield strength is increased to 19.3 MPa (2800 psi), and further irradiation to 10^7 R has elevated the yield strength to 47.2 MPa (6850 psi). This rate of hardening with irradiation exposure is consistent with that observed by Nadeau.[10]

Fracture-toughness measurements were also conducted on several bars to determine the effective surface energy for crack propagation on the main cleavage plane, {100}. The bars were loaded as double cantilever beam specimens according to the method described by Hoagland, et al.[11] These data, together with the flow properties, are compiled in Table 1. These effective energies may be compared with the value of 0.34 J/m^2 measured by Gilman[12] at -196 C, a value that is probably close to the

*The principal slip system in LiF (which has an NaCl crystal structure) at room temperature is in the $\frac{a}{2}$ <110> directions on the {110} planes. At higher temperatures slip may occur in the $\frac{a}{2}$ <100> directions.

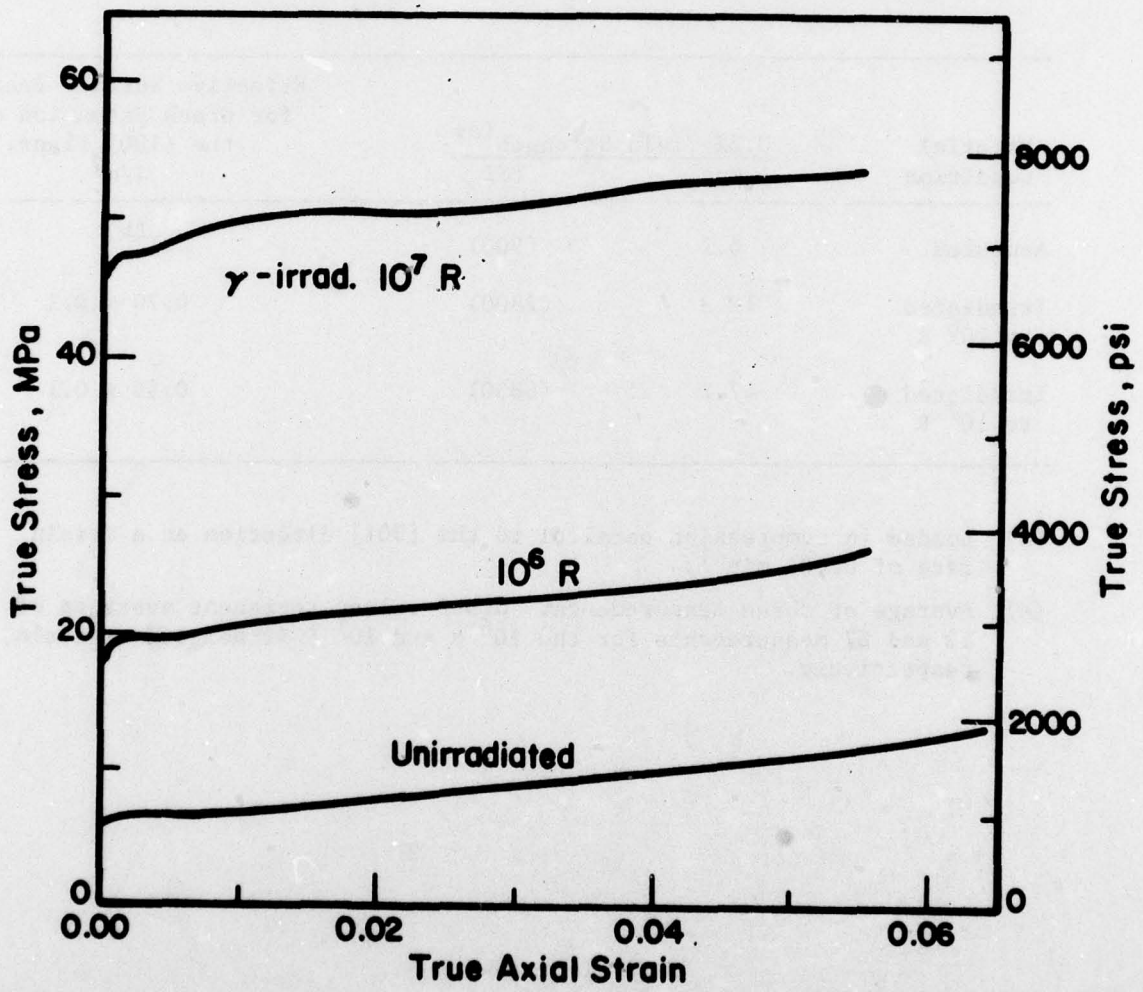

FIGURE 1. FLOW CURVES IN COMPRESSION OF THE LiF SINGLE-CRYSTAL MATERIALS USED IN THIS STUDY

Compression was applied along a <100> direction to square-cross-section specimens approximately 12.7 mm long by 4.4 mm on a side. Strengthening of the crystals was accomplished by γ-irradiation from a ^{60}Co source to the levels shown.

TABLE 1. MECHANICAL PROPERTIES OF THE LiF SINGLE-CRYSTAL MATERIAL AT 25 C

Material Condition	0.2% Yield Strength[a] Mpa	PSI	Effective Surface Energy for Crack Extension on the (100) Plane, J/m^2
Annealed	6.2	(900)	2.1[b]
Irradiated to 10^6 R	19.3	(2800)	0.70 ± 0.1
Irradiated to 10^7 R	47.2	(6850)	0.55 ± 0.1

(a) Loaded in compression parallel to the [001] direction at a strain rate of 0.004 min^{-1}.

(b) Average of three measurements. Other values represent averages of 12 and 67 measurements for the 10^6 R and 10^7 R irradiated crystals, respectively.

true surface energy of LiF. Thus, a substantial portion of the energy dissipated in cleavage of these crystals is consumed by plastic deformation. The reduction in effective surface energy with irradiation is a simple consequence of the increased resistance to dislocation glide. The important point to be noted is that the properties of these crystals form a rather broad range of combinations of strength and toughness covering an 8-fold range in flow strength and a 4-fold range in fracture toughness.

In preparation for impacting, specimens shaped approximately as cubes with a side length of 5 mm were cleaved from stock. The specimens were first etched in Gilman's "A" etch[13] and the surface to be impacted was photographed to characterize the preexisting dislocation distribution. After impacting, the specimens were again etched and the impacts located and photographed. This procedure also permitted identifying those pre-existing dislocations which moved during the impacting events because the new dislocation location is marked by a smaller-size pit and the old location is occupied by a flat-bottomed pit.

2.2. Impingement Procedure

The vacuum chamber within which the test specimens were impacted is shown in Figure 2. In this chamber, the specimen was attached to a steel rotor arm and rotated at the desired speed. The selection of a monolithic tapered rotor arm, Figure 3, instead of a more easily balanced disc, was guided by the potential for high stresses likely to arise in a specimen holder which must necessarily protrude from the surface or edge of a disc. The arm is tapered to reduce the radial stresses near the axis of rotation. The center of the specimen seated within the square hole in the end of the arm was located 15.6 cm from the axis of rotation. This length together with the taper angle determines the length of the short stem of the arm necessary to achieve balance. In addition, to balance the added weight of the specimen, which may vary from one specimen to another, a cup was bored into the short end to receive counterbalance masses. With this design, excellent static and dynamic balance was achieved. The arm was rotated by means of a high-speed 0.75-hp motor mounted outside the chamber, turning the shaft through a rotatable vacuum feed-through. Some problems were encountered in the design of the bearings in this feed-through which currently limit the rotational speed to about 10,000 rpm.

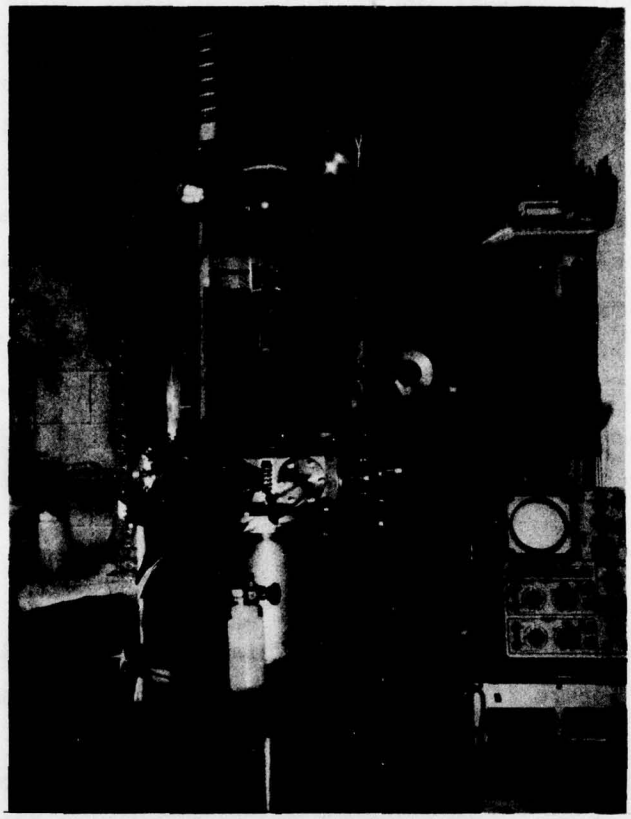

FIGURE 2. HIGH SPEED DROPLET IMPACT DEVICE

The three-piece vacuum chamber is shown. The bottom section is a length of line pipe approximately 15 mm thick within which the rotating arm is attached. Droplets are produced from an oscillating stream issuing from a hypodermic needle mounted to the assembly visible within the bell jar.

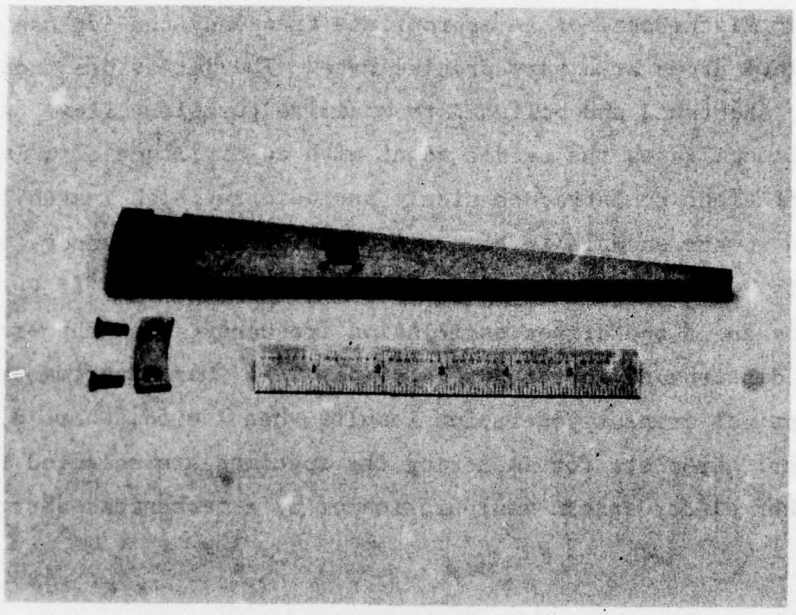

FIGURE 3. ROTATING ARM ASSEMBLY

The specimen is mounted in the rectangular hole near the narrow end of the arm approximately 156 mm from the axis of rotation. A cup for counterbalance weights is located in the opposite end of the arm.

With improved design (in progress), rotational speeds to 30,000 rpm and larger may be obtained without exceeding the failure stress in the arm.

The method for generating drops with precisely controlled size has been described in detail by Lindblad and Schneider.[14] The method relies on the Rayleigh instability which occurs in a liquid jet brought about when the jet begins to neck down and pinch off into a drop under the action of surface tension. Any randomly occurring disturbance might initiate the instability; therefore, by introducing a high-amplitude periodic disturbance of an appropriate frequency the jet can be made to pinch into drops at a very precise rate. The jet issues from a hypodermic needle, shortened and polished to minimize turbulent flow. A piezoelectric crystal oscillates the needle mount with an amplitude of only a few microns but sufficient to introduce nicely periodic Rayleigh instabilities, as can be seen in the example in Figure 4. The optimal frequency for generating droplets depends upon the flow rate and jet diameter. If V is the jet velocity and f the driven oscillation frequency, then the wavelength, λ, of the disturbance in the jet is simply V/f. Our experiments indicate that optimal droplet generation results when $\lambda = 5d$, where d is the jet diameter. Droplets for impacting the specimen are selected from the stream by either electrostatic manipulation or by a mechanical shutter.

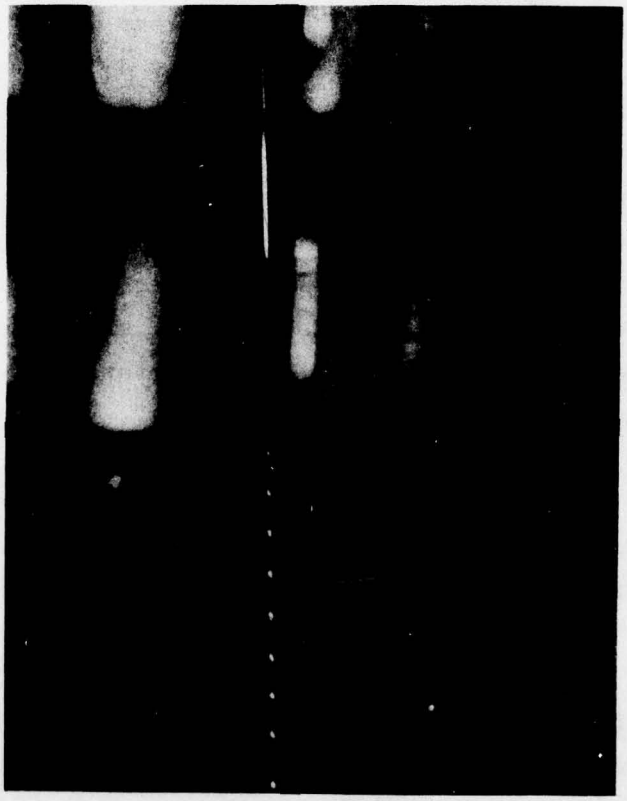

FIGURE 4. DROPLETS FORMING FROM AN OSCILLATING STREAM OF WATER

The droplets have a diameter of 0.4 mm and are being produced at a rate of 3000 per second.

3. NUMERICAL MODELING OF THE DROPLET IMPACT EVENT

Numerical simulation is a valuable tool for quantatively examining important aspects of an impact event. In particular, pressure, velocity and stress distribution can be watched as the impact develops. Of the several numerical treatments of fluid impact on solid surfaces, the recent work of Rosenblatt, et al.[7,8] involves one of the most finely divided computations so far conducted. Perhaps as a consequence their calculations predict larger peak pressures than previous numerical models. Because the results described in the next section point to the existance of pressures significantly larger than predicted by Rosenblatt, et al, we undertook a calculation of the very early stages of the impact in a model which was much more finely divided than that of Rosenblatt, et al. The calculation was done using the hydrodynamic code HELP, a two-dimensional code which solves the equations of motion of incremental elements of the body by finite differences in Eulerian coordinates. A complete description of the HELP code is contained in Reference (15).

The model considered the impact of a spherical 0.4 mm-diameter water droplet with a lithium fluoride solid at 100 m/s. The water and lithium fluoride were subdivided into meshes with nonuniform dimensions in both the direction along the axis of collision and radially away from the point of first contact. The smallest meshes were located near the point of first contact and Figure 5 shows the overall subdivision scheme for the water and lithium fluoride. At the beginning of the calculation the time increment was only 2×10^{-13} sec. This increment was doubled with each passing time step up to a point where the time increment was determined by the wave speed. The criterion setting the time increment then became equal to 40 percent of the shortest elapsed time for the passage of a dilatation wave across a grid. Typically, this increment was about 2.2×10^{-11} secs. for the remainder of the calculation.

The equation of state for water was taken from Hwang and Hammitt[6] with the form of the expression modified for use in the HELP code and also included the contribution from the adiabatic change in internal energy. Under compression the pressure is given by

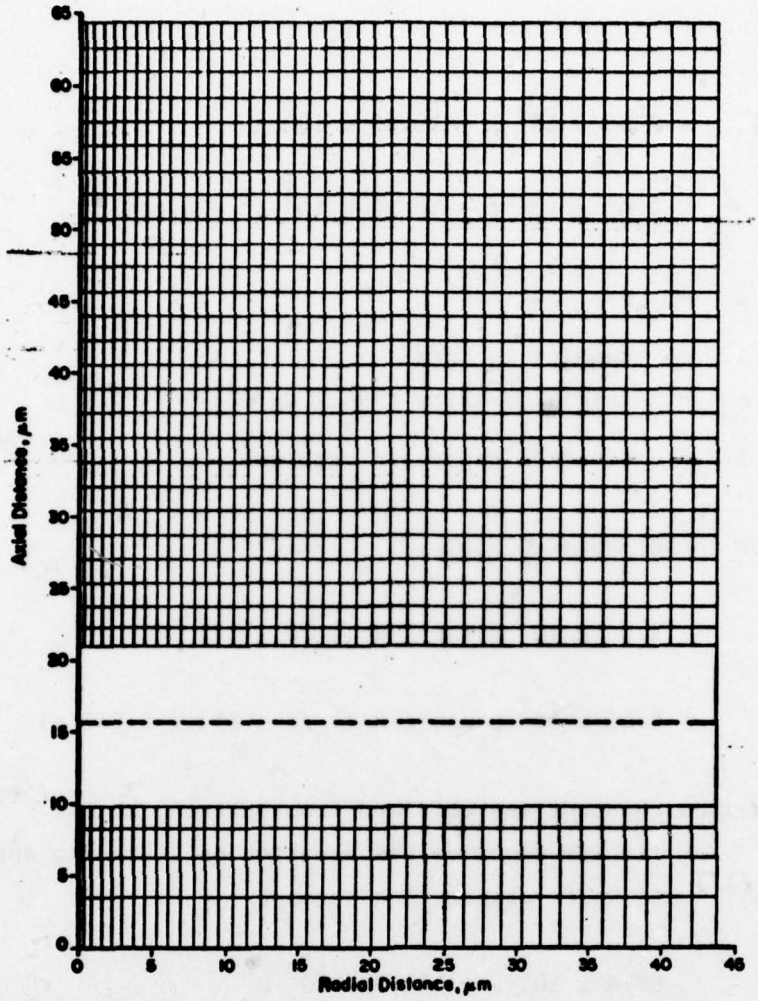

(a)

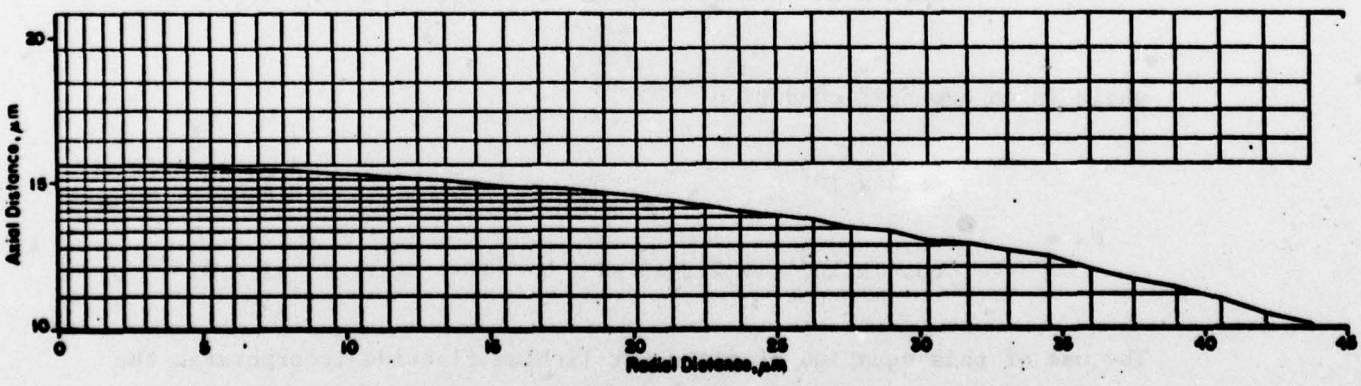

(b)

FIGURE 5. THE MESH NETWORK EMPLOYED IN THE NUMERICAL MODEL OF A 0.4 MM DIA. SPHERICAL WATER DROP IMPACTING A FLAT LITHIUM FLUORIDE SURFACE AT 100 M/S. The interface is initially at 16mm separating the water drop below and the lithium fluoride above. In (a) is shown the mesh spacing exclusive of the area containing the interface, while the more finely divided meshes in the immediate vicinity of the contact point are shown in (b)

$$P = \begin{cases} 2.03 \times 10^9\ \mu + 10.29 \times 10^9\ \mu^2 & I < 0 \\ 2.03 \times 10^9\ \mu + 10.29 \times 10^9\ \mu^2 + 0.045\ \rho I & I > 0 \end{cases}$$

where $\mu = \rho/\rho_o - 1$

ρ = density in kg/m^3

ρ_o = initial density (998.2 kg/m^3)

I = internal energy in ergs/g

For water in an expanded state

$$P = \begin{cases} 2.03 \times 10^9\ \mu \exp\left[-2\ (\rho_o/\rho - 1)\right] & I < 0 \\ 2.03 \times 10^9\ \mu \exp\left[-2\ (\rho_o/\rho - 1)\right] + 0.045\ \rho I & I > 0 \end{cases}$$

The Gruneisen constant was obtained from Gurtman, et al.[16]

For lithium fluoride the equation of state was adapted from Bridgman[17] and under compression becomes

$$P = \begin{cases} 68.4 \times 10^9\ \mu + 183.9 \times 10^9\ \mu^2 & I < 0 \\ 68.4 \times 10^9\ \mu + 183.9 \times 10^9\ \mu^2 + 0.045\ \rho I & I > 0 \end{cases}$$

while in an expanded condition

$$P = \begin{cases} 68.4 \times 10^9\ \mu & I < 0 \\ 68.4 \times 10^9\ \mu + 0.1343\ \rho I & I > 0 \end{cases}$$

The use of this equation of state for lithium fluoride incorporates the assumption that the lithium fluoride behaves as an isotropically elastic solid, i.e., neither the flow strength nor the anisotropy of this material enters the calculation.

4. RESULTS

In some cases, the deformation produced by the impact is observable as a rosette of small, but resolvable, dislocation etch pits. Because each crystal was etched both prior to and after impact, the larger pits evident in the following micrographs mark the locations of dislocations that were present prior to impact. As a guide to assist in interpreting the rosettes and the orientations of the slip planes comprising the patterns, the deformation around an indentation caused by a steel ball is shown in Figure 6. The schematic shows the slip planes making up the pattern and illustrates the sense of slip on each plane necessary to accommodate the stresses. Representative photo-micrographs of damage sites caused by impact of 0.4-mm-diameter water drops are shown in Figure 7, 8, and 9 for the unirradiated, the 10^6 R irradiated, and 10^7 R irradiated crystals, respectively.

These observations reveal a characteristic feature of the impact damage, namely a very localized area of a size considerably smaller than the droplet. In addition, the shape and size of the dislocation array marking the impact site is quite variable, even under what should be identical conditions, e.g., material, impact velocity, and drop size. These and additional findings are described in greater detail below.

4.1. Discrepancy Between Number of Impacts Observed and Predicted

Typically each specimen was subjected to 50 to 300 impacts. This procedure was adopted after several attempts at finding damage produced by single impacts failed. On the average, the number of observable rosettes was only about one-tenth the estimated total number of impacts. However, there is a degree of uncertainty concerning the total number of impacts due primarily to some slight air movement in the chamber which slightly disturbs the path of the droplets as they fall to impact the specimen. As a consequence, some droplets may not intersect the central portion of the specimen. Nevertheless, considering the wide variability in the size and shape of observable impact sites, there exists the possibility that some impacts do not produce a local damage zone. There is, in fact,

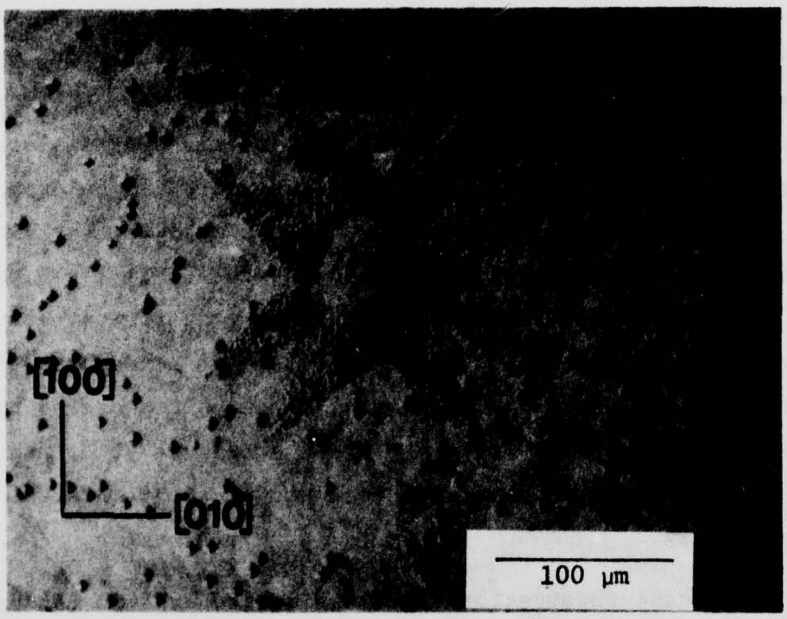

a. Deformation pattern resulting from indentation of a 1-mm-diameter steel ball loaded to 190 grams in a (001) plane

FIGURE 6. ORIENTATION OF SLIP PLANES AND DIRECTION OF SLIP CAUSED BY HERTZIAN STRESSES

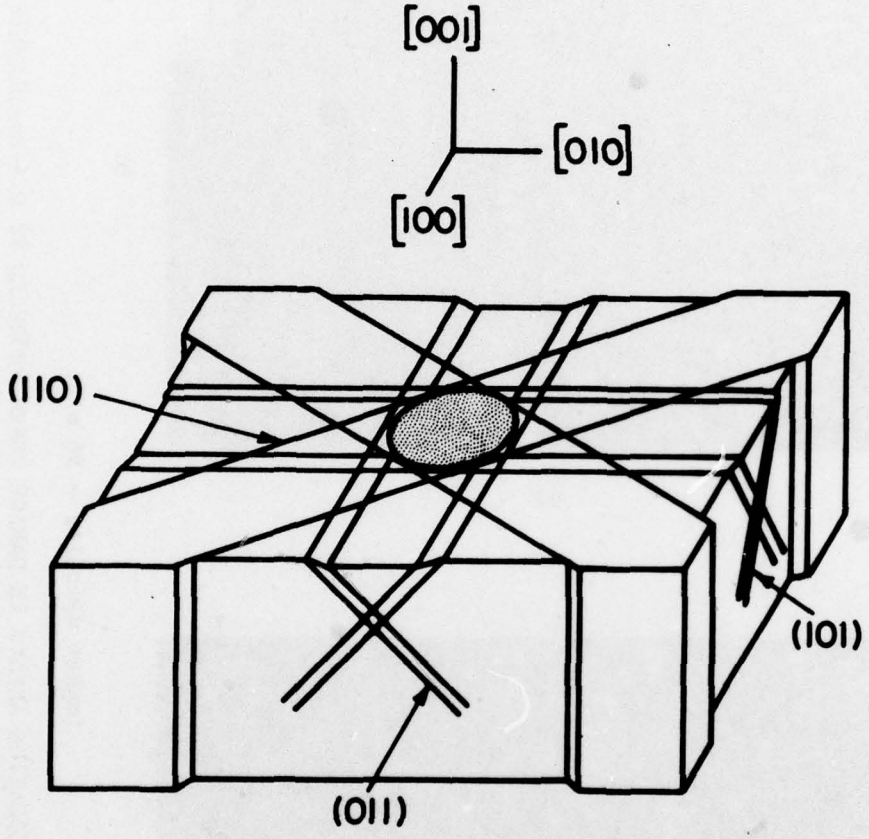

b. A schematic of the pattern in (a) showing the orientation of the six slip planes and the slip directions accommodating the plastic deformation

FIGURE 6. (Continued)

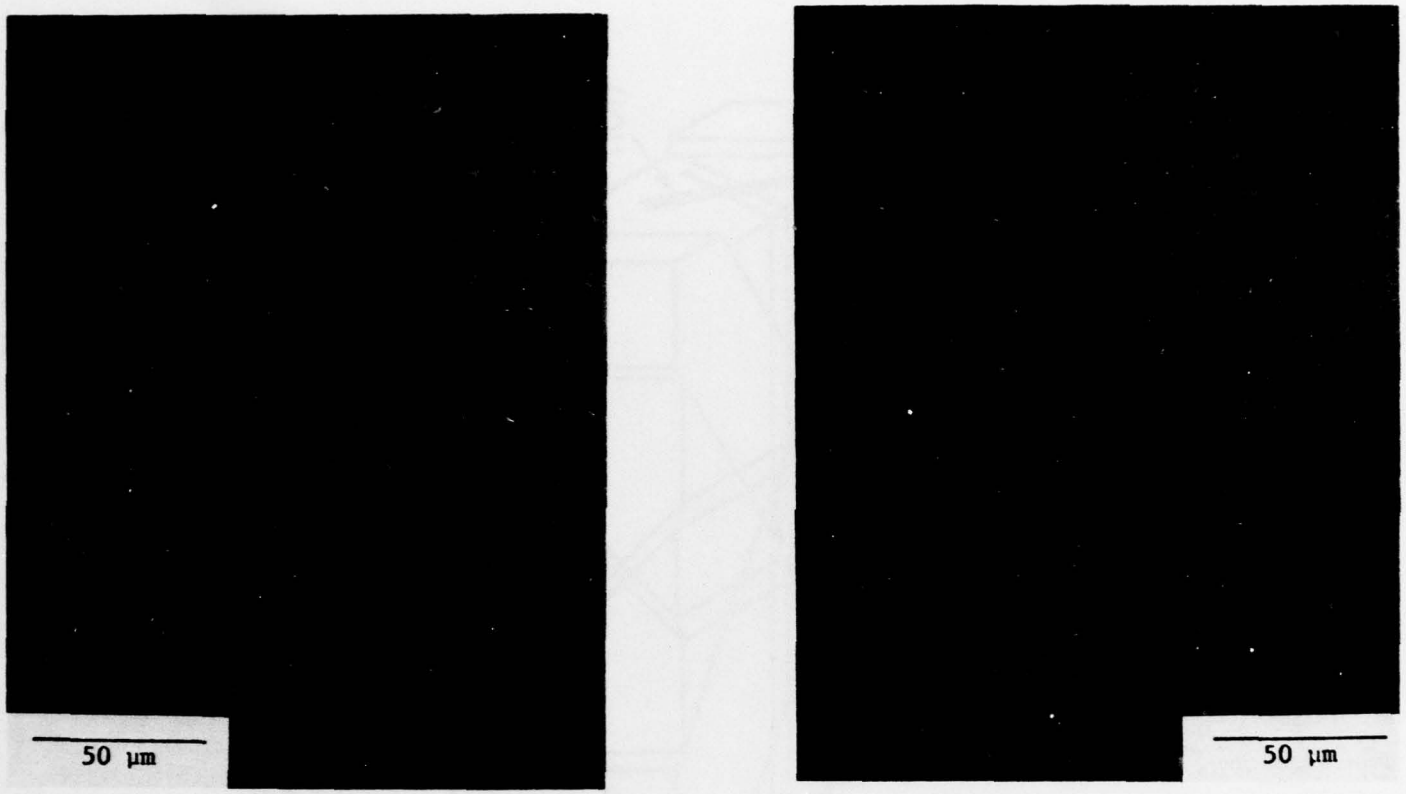

a. b.

Impact velocity = 96 m/s.

FIGURE 7. EXAMPLES OF DISLOCATION ARRAYS IN DAMAGE ZONES PRODUCED BY 0.4-mm-DIAMETER WATER-DROPLET IMPACTS ON UNIRRADIATED LITHIUM FLUORIDE

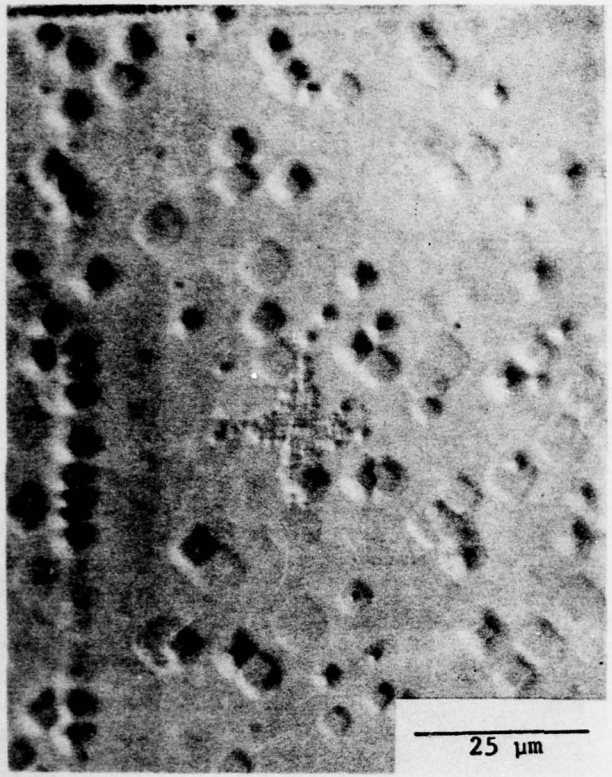

c.

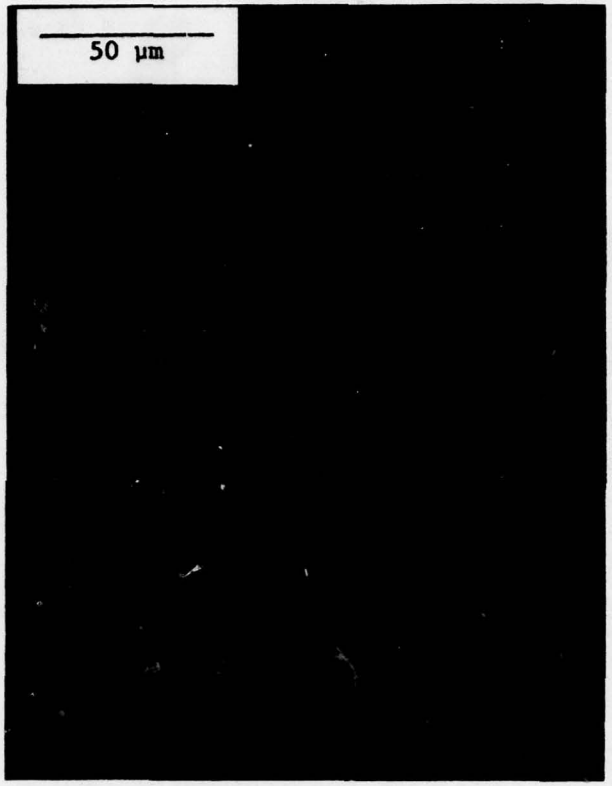

d.

Impact velocity ≈ 96 m/s.

FIGURE 7. (Continued)

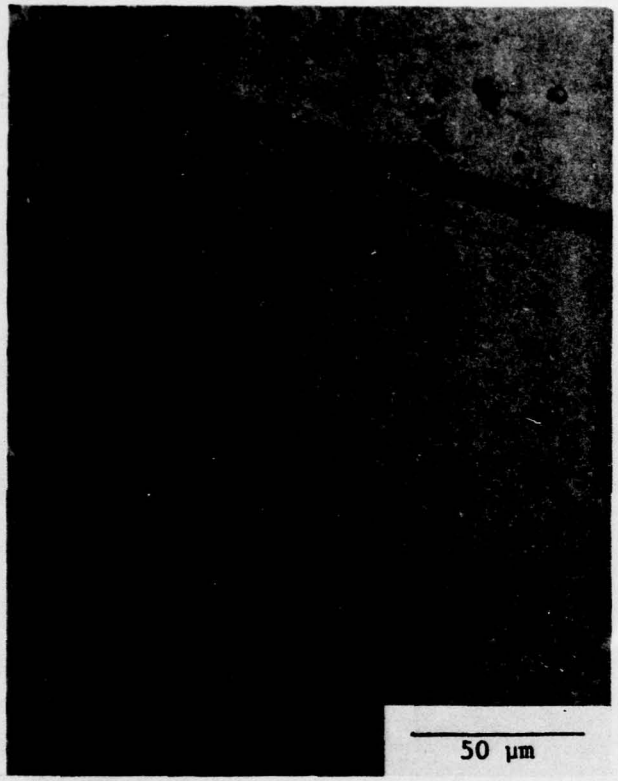

e.

f.

Impact velocity = 130 m/s.
Note also in (f) the flat-bottomed etch pits.

FIGURE 7. (Continued)

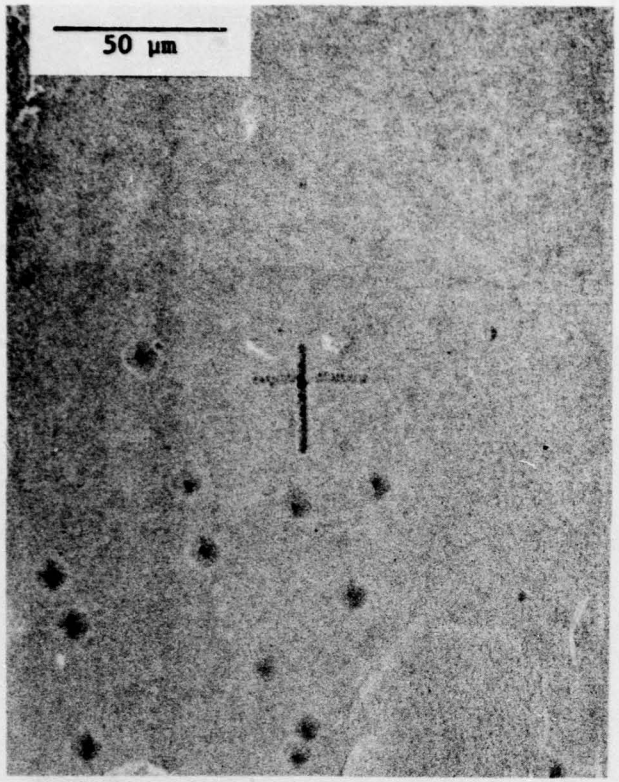

a.

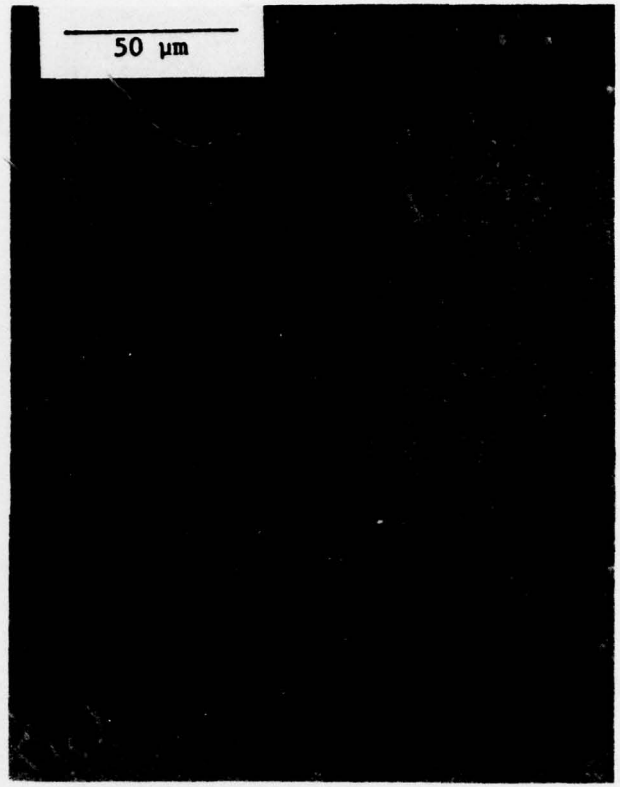

b.

FIGURE 8. EXAMPLES OF DISLOCATION ARRAYS IN DAMAGE ZONES PRODUCED BY 0.4-mm-DIAMETER WATER-DROPLET IMPACTS AT 96 m/s ON LITHIUM FLUORIDE γ-IRRADIATED TO 10^6 R

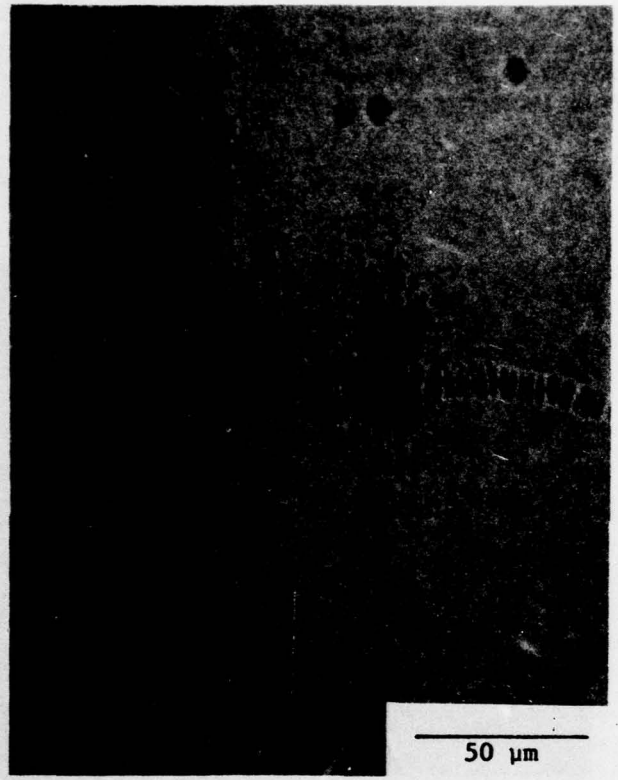

c.

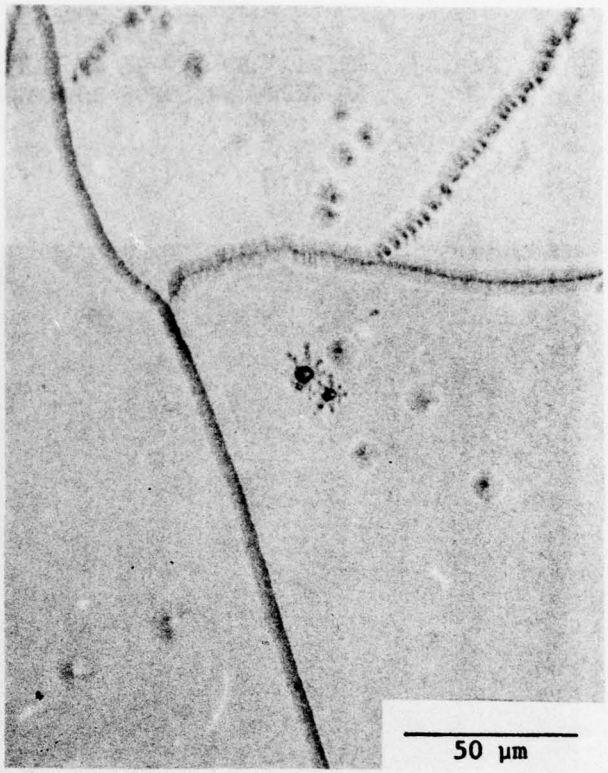

d.

FIGURE 8. (Continued)

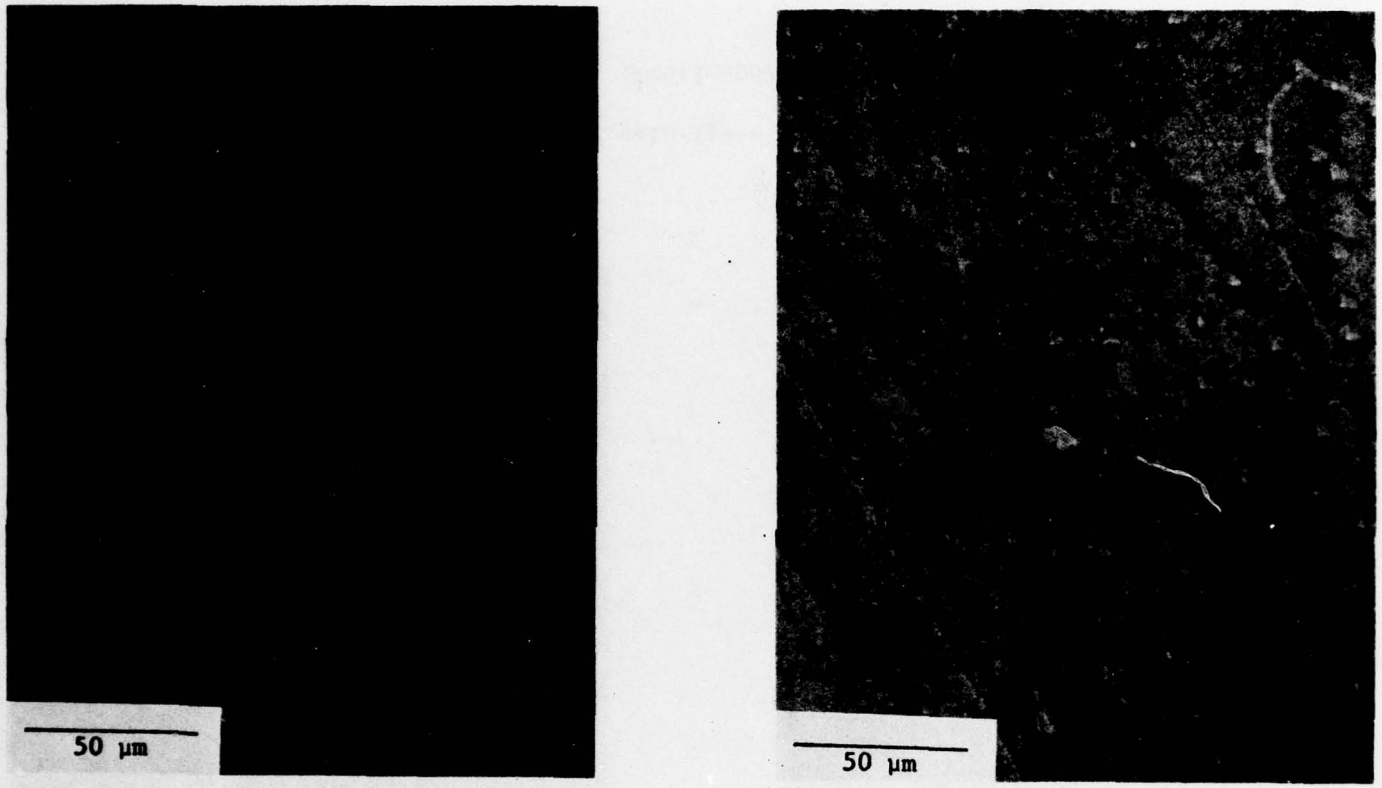

a. b.

Impact velocity = 96 m/s.

FIGURE 9. EXAMPLES OF DISLOCATION ARRAYS PRODUCED BY 0.4-mm DIAMETER WATER-DROPLET IMPACTS ON LITHIUM FLUORIDE γ-IRRADIATED TO 10^7 R

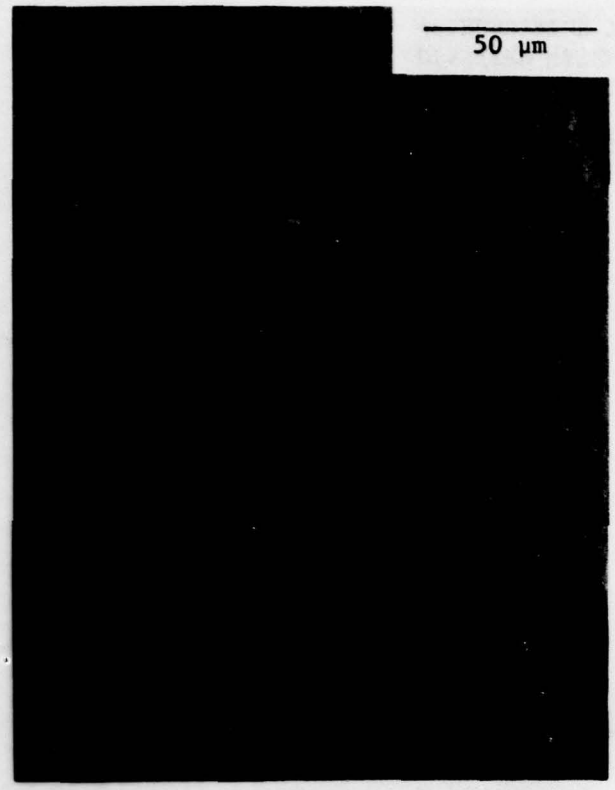

c.

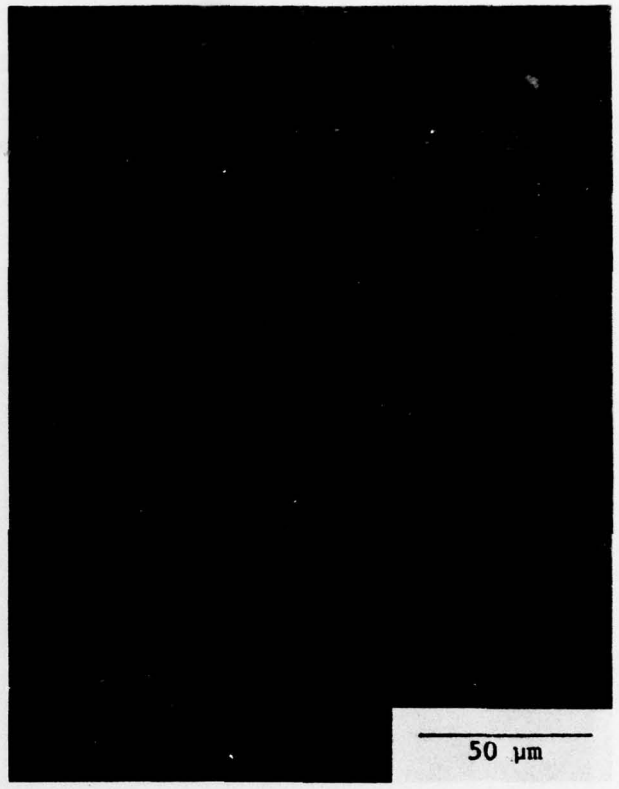

d.

Impact velocity = 96 m/s.

FIGURE 9. (Continued)

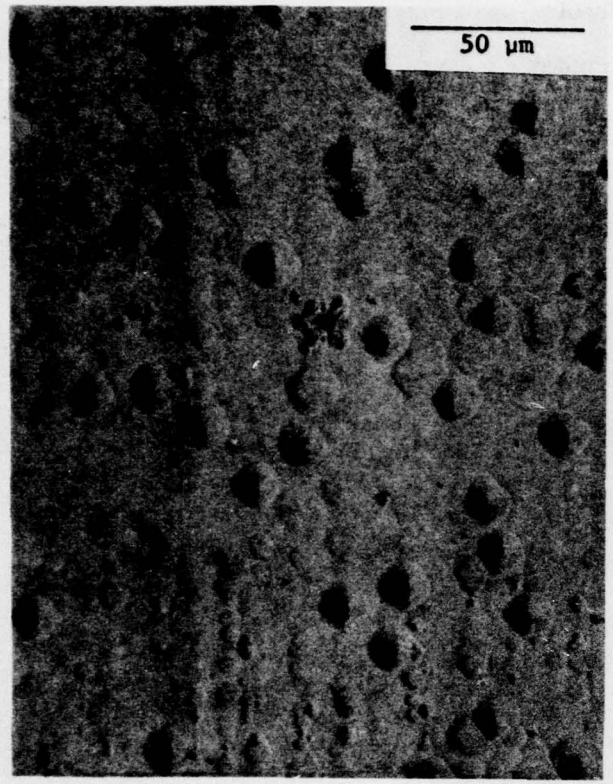

e.

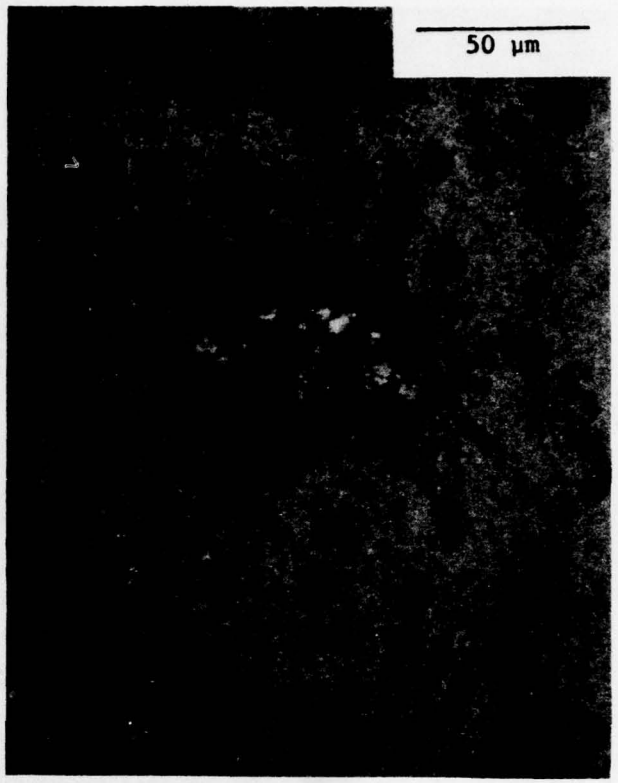

f.

Impact velocity = 160 m/s.

FIGURE 9. (Continued)

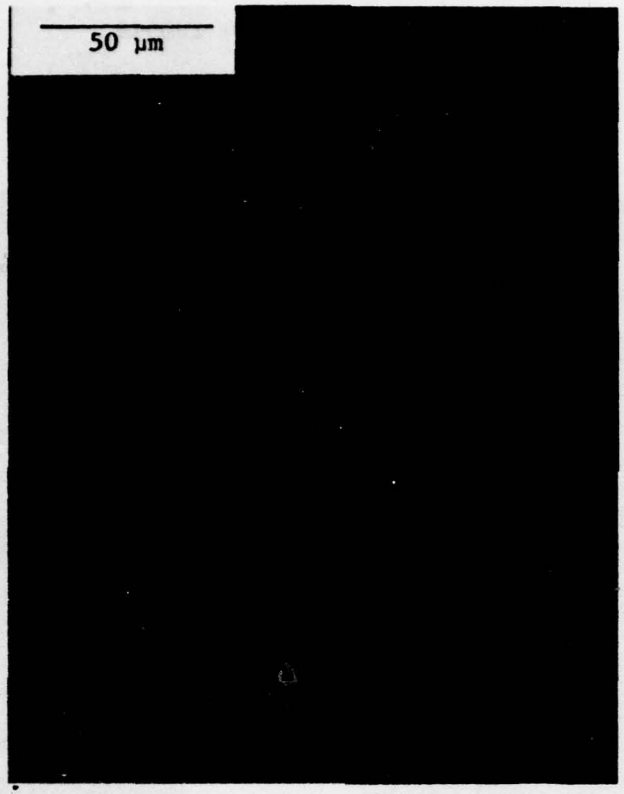

g.

Impact velocity = 160 m/s.

FIGURE 9. (Continued)

evidence of other forms of damage as discussed below. To ensure that the damage was not due to solid particle impact (e.g., with dust particles) several specimens were run for long periods, ∿ 300 seconds, in the absence of water droplets. Complete examination of the surfaces of these "dry run" specimens did not reveal new impact damage.

4.2. Cratering

In certain but not all impacts a central region of intense damage is apparent. Examples of intensely damaged zones are presented in Figures 7b, 8b, 8d, 93, and 9f. It appears that the intensely damaged zones are craters resulting from a small amounts of material torn from the surface. A very clear example of a crater is evident in Figure 9f, which shows a site produced by a 0.4-mm-droplet impacting at 160 m/s on a crystal of the 10^7 R irradiated material. There is also evidence of several cracks on {110} planes emanating from the crater. Even at this higher impact velocity, however, *a central crater* was not always produced, as Figure 9g shows.

4.3. Dislocation Punching

In Figure 9c, two very small dislocation clusters are evident. In one, four etch pits are resolvable; in the other, six. Our interpretative of this arrangement is that the clusters are composed of dislocation loops, as picture schematically in Figure 10a. These loops lie along the {110} planes inclined at 45 degrees to the surface (cf. Figure 6b). Similarly, the larger damage zones are also thought to be composed of more numerous dislocation loops nestled one within another, as suggested by the drawing in Figure 10b.

In most cases the design zone at an impact site is apparently produced in the absence of preexisting dislocations. Prior to an impact run, the surface of each specimen is completely surveyed and photographed so that the location of all preexisting dislocations and other surface defects are identified. The pre- and postimpact surfaces are then compared to ascertain the condition of the surface at the location of each damage site. These results show that, with rare expection, the damage is produced on a flat area previously unoccupied by dislocations. This is a

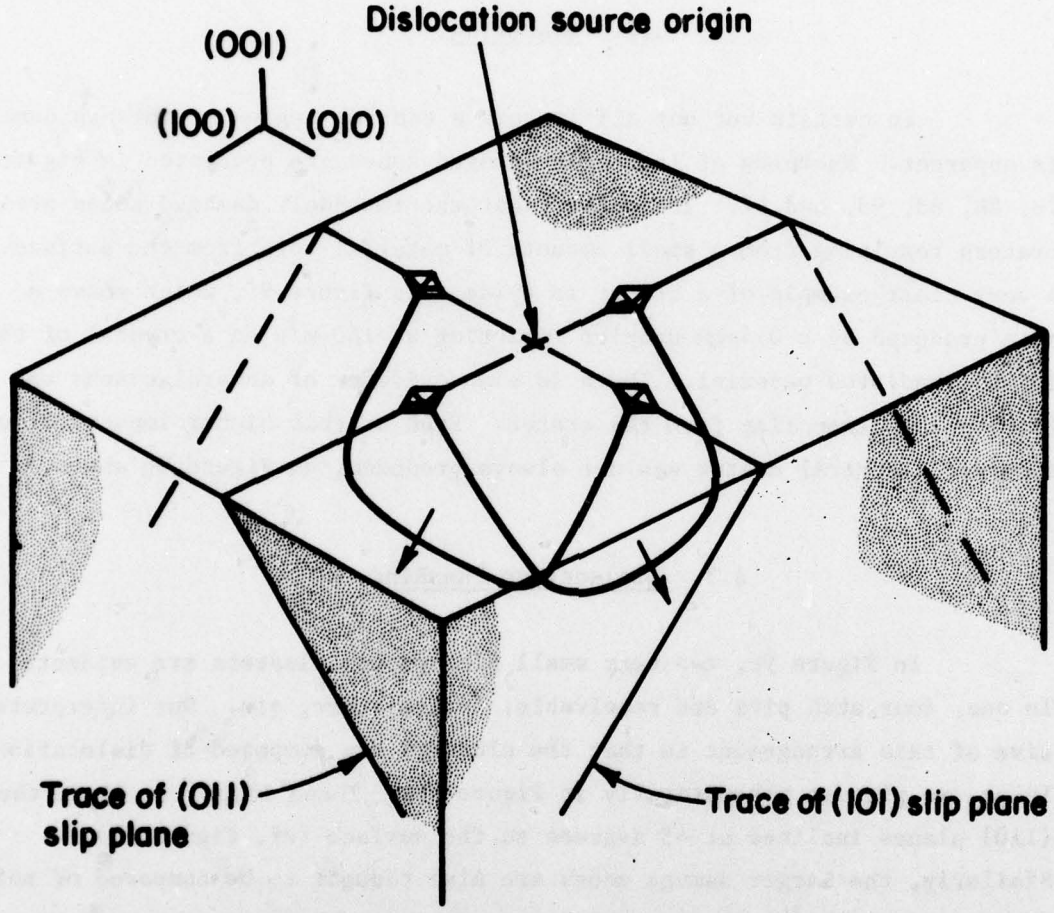

a. Simple four-etch-pit, two-loop arrangement suggested dislocation-cluster-pattern in Figure 9c

FIGURE 10. SCHEMATICS OF PROBABLE DISLOCATION-LOOP ARRNAGEMENT

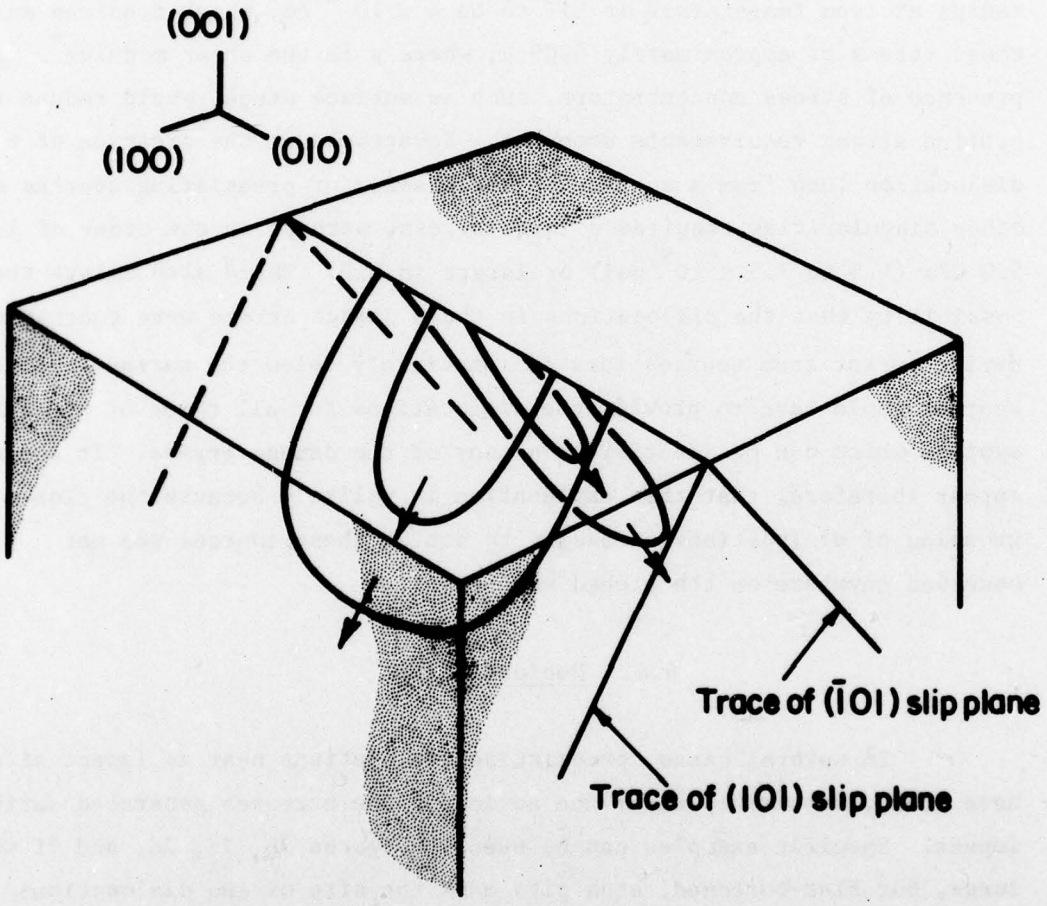

b. More complex loop arrangement consisting of nested loops lying along complementary slip planes, for clarity, loops on the other pair of complementary slip planes are not shown.

FIGURE 10. (Continued)

significant point, because it suggests that stresses sufficient to punch in dislocations were required to produce these new arrays. The shear stresses necessary to accomplish this task may be quite large as the analysis by Hirth[18] indicates. He derives the strain energy and, therefore, the shear stress needed to produce a critical-size dislocation loop at a free surface. With further increase in the radius of the loop, its energy decreases. From Hirth's analysis we estimate the critical loop radius at room temperature in LiF to be 4×10^{-8} cm, which requires an applied shear stress of approximately 0.09 μ, where μ is the shear modulus*. The presence of stress concentrators, such as surface steps, would reduce the applied stress requirements somewhat. Nevertheless, the creation of a dislocation loop from a surface in the absence of preexisting sources or other singularities requires a large stress, perhaps on the order of 1.0 to 5.0 GPa (1.5 to 7.5×10^5 psi) or larger in LiF. There also exists the possibility that the dislocations in these damage arrays were generated during impact from sources located immediately below the surface. Such sources would have to provide the dislocations for all three of the slip systems which can be identified in many of the damage arrays. It would appear therefore, that this explanation is unlikely because the close grouping of dislocations necessary to act as these sources was not observed anywhere on the etched surfaces.

4.4. Nonlocal Slip

In several cases, preexisting dislocations near an impact site have moved, presumably under the action of the stresses generated during impact. Specific examples can be seen in Figures 7b, 7c, 7d, and 7f where large, but flat-bottomed, etch pits mark the site of the dislocations present prior to but not after impact. In this regard it is interesting

---

*The analysis due to Hirth is for an elastically isotropic solid. The appropriate shear modulus for LiF, an elastically anistotropic solid, may be estimated from the Voight average of the elastic constants, C_{11}, C_{12}, and C_{44}, as $\mu = 1/5\ (3C_{44} - C_{12} + C_{11})$. From the Landolt-Bornstein[22] Tables, $C_{11} = 11.2$ GPa, (16.13×10^6 psi), $C_{12} = 42$ GPa (6.1×10^6 psi), and $C_{44} = 62.8$ GPa (9.11×10^6 psi) which gives $\mu = 51.5$ GPa (7.47×10^6 psi).

to note that several areas could be found where a relatively substantial fraction of the preexisting dislocations had moved even though a damage site could not be found in the immediate vicinity. Figure 11 shows an example of a region on an unirradiated specimen following impact where a large number of preexisting dislocation etch pits are flat bottomed and numerous small pits marking new dislocation positions can be seen. Preexisting dislocations which had moved during impact were observed primarily in the unirradiated material, rarely in the 10^6 R material, and never in the highest strength, 10^7 R material. This observation suggests that some impacts produce relatively low-level stresses which are sufficient to move preexisting dislocation but insufficient to generate the tightly clustered array of new dislocations.

4.5. Damage-Zone Size Distribution

Damage-zone diameters were measured for each strength level and impact velocity. These diameters were obtained from the average of two orthogonal measurements of the maximum extent of the dislocation distribution at each impact site. A large spread in damage-zone sizes is evident. One possible way of representing the distribution function describing the probability of finding a damage-zone diameter between y and y + dy is

$$f(y)dy = \frac{1}{\sqrt{2\pi}\sigma} \exp\left[\frac{-(y - \bar{y})^2}{2\sigma^2}\right] . \qquad (2)$$

Equation (2) is the Gaussian or normal distribution function with $\bar{y}$ the mean value of y, and σ, the standard deviation of y. Clearly, from a physical standpoint, Equation (2) is inappropriate for describing the distribution of the damage zone diameters because it admits the possibility of negative diameters. A better representation is, in fact, the log-normal distribution, produced by replacing y by ℓn y in Equation (2). The cumulative distribution function, defined formally by

$$P(y) = \int_{y_1}^{y_2} f(y)\, dy \quad , \qquad (3)$$

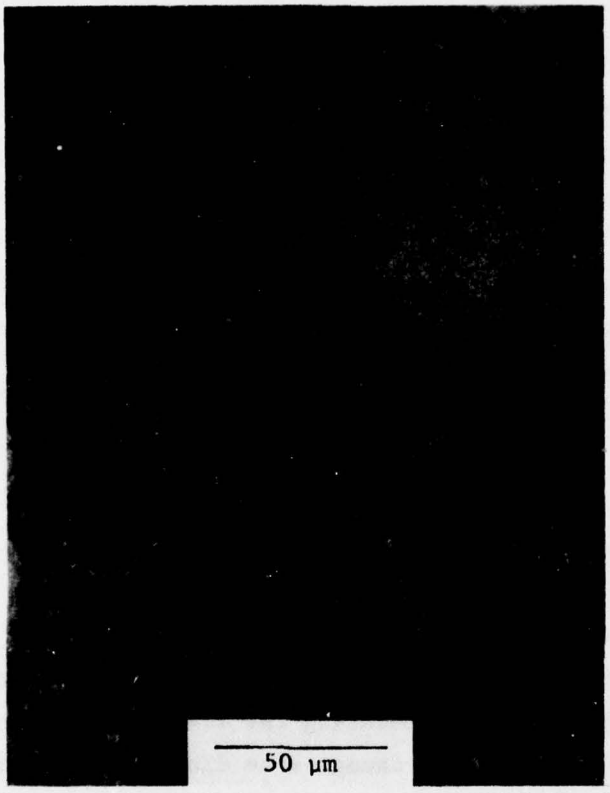

FIGURE 11. A FIELD OF PREEXISTING DISLOCATIONS

Most of the dislocations are flat bottomed indicating that they have moved. Numerous small etch pits generated during impacting are also evident. Unirradiated specimen impacted with 0.4-mm-diameter droplets at 96 m/s.

represents the fraction of the population between y_1 and y_2. It is convenient to test the suitability of the log-normal distribution for these samples by plotting the cumulative distribution function against ℓn y; Figure 12 shows this plot on a logarithmic probability scale for the 96 m/s results. Except for the largest damage zones in the lower strength materials, the nearly linear relation between ℓn y and P(y) on this graph confirms the applicability of the log-normal distribution function representing these data.

The plot also demonstrates several additional points. The median damage-zone diameter* is only 6 μm in the 10^7 R material, but in both the unirradiated and 10^6 R specimens the median damage-zone diameters are 17 μm and 16 μm, respectively. In fact, the unirradiated and 10^6 R specimens display essentially identical distributions, and therefore identical response to water-droplet impact at 96 m/s. This is a rather surprising result but seems to indicate that the bulk flow properties may not be entirely adequate parameters for predicting resistance to deformation during impact. For example, there exists the possibility that the defect concentration (produced by the gamma irradiation) is lower near the surface than internally. As a consequence, in the 10^6 R material the defect concentration may be sufficiently low near the surface that it responds to the droplet impact, plastically, like the defect-free, unirradiated material.

Finally, we should expect the damage size distributions to possess a lower bound diameter. On reason for this is, of course, simply the limits imposed by our ability to optically resolve individual dislocations in the damage cluster. A second reason centers on the possible reversibility of the damage. It was suggested earlier that the dislocations comprising the damage zone are probably loops. If the loops formed by an impact are sufficiently small, they will collapse back to the surface under the action of their line tension. We can obtain an estimate of the relation between loop size and the shear stress necessary to sustain the loop from the relation for the self-energy per unit length of a loop given by Nabarro[16],

*The diameter at which P(y) = 50 percent.

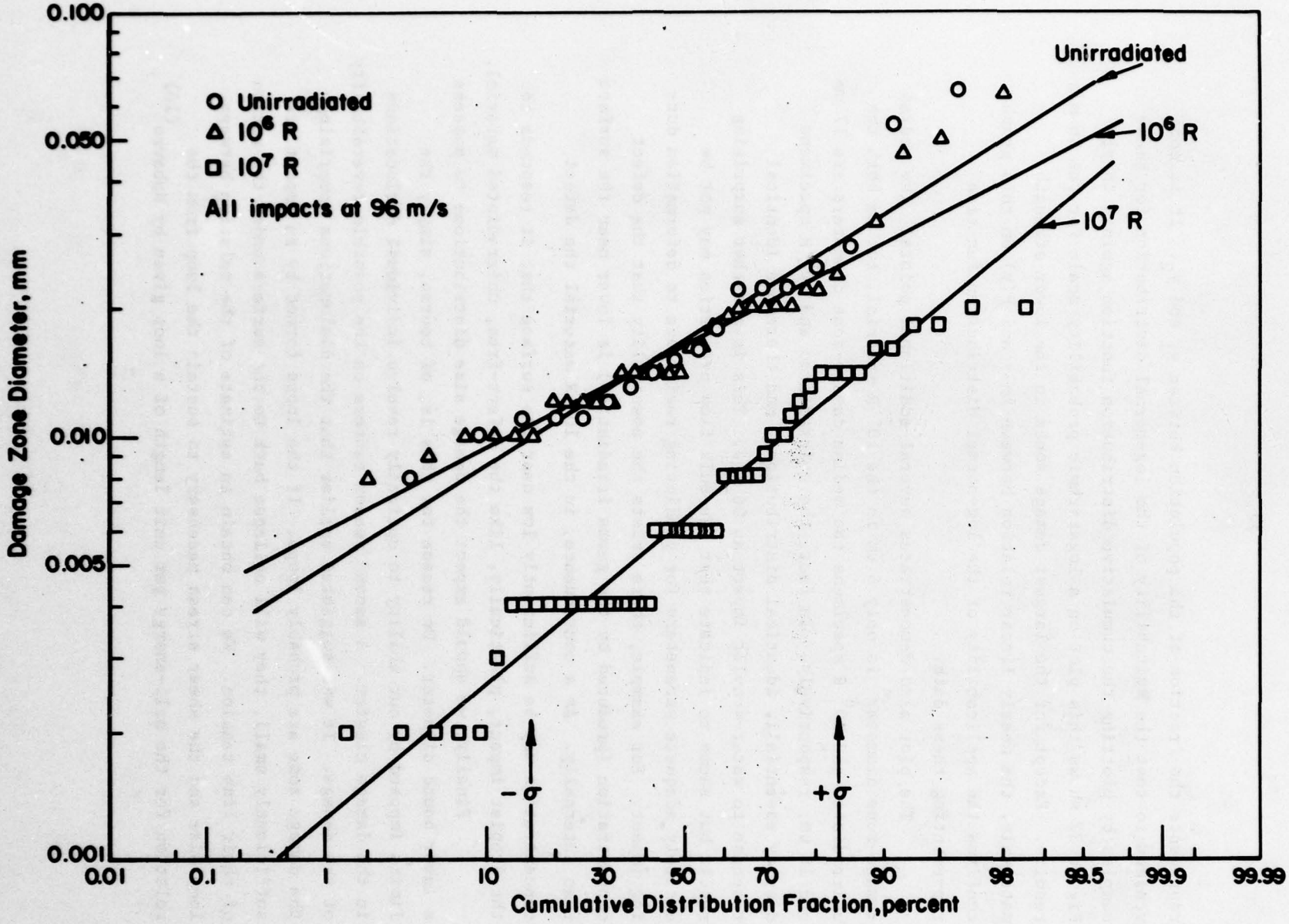

FIGURE 12. THE LOG-NORMAL CUMULATIVE PROBABILITY DISTRIBUTION OF DAMAGE-ZONE SIZES FOR 96 m/s IMPACT OF 0.4-mm-DIAMETER DROPLETS

The damage-zone sizes have an estimated measurement accuracy of about ±0.001 mm.

$$\frac{W}{L} = \frac{\mu b^2 (2 - \nu)}{8\pi (1 - \nu)} \ln \frac{4R}{\rho} \quad , \tag{4}$$

where b is the dislocation Burgers vector, R is the loop radius, and ρ the cutoff distance, $\rho \simeq b$. The shear stress to support a loop of radius R is obtained from

$$\tau b = \frac{d}{dR}\left(\frac{W}{L}\right) \quad ,$$

giving

$$\tau = \frac{\mu b}{8\pi R} \frac{(2 - \nu)}{(1 - \nu)} \quad . \tag{5}$$

If we take $\tau = \tau_c$, the critical resolved shear strength of the crystal, Equation (5) provides an estimate of the minimum size loop that would be stable in an unstressed crystal. Taking $\tau_c = 3.1$ MPa (450 psi), the critical resolved shear stress of the unirradiated material, gives a minimum loop radius of 0.4 μm. Although this estimate of minimum loop size is somewhat smaller than that observed in either the irradiated or unirradiated material, it provides a physical basis for expecting a nonzero lower limit to the damage zone sizes. Furthermore, it indicates that the damage-zone sizes, resulting from impacts under ostensibily identical conditions, probably vary by two orders of magnitude or more.

4.6. Relation Between Impact Damage and Impact Velocity and Flow Strength

The variation of the damage-zone sizes with bulk yield strength and impact velocity for impacts by 0.4-mm-diameter droplets are summarized in Table 2. Graphic representations of these results showing the variation in damage-zone size with bulk yield strength at an impact velocity of 96 m/s is given in Figure 13, and the dependence on impact velocity in Figure 14. As defined in the previous section, the median values divided each data group into two equal parts. The standard deviations are obtained by fitting the data distribution to a log-normal distribution. The fact that the upper and lower bounds of the standard deviations are not equal is evidence of the skewness of the data about the mean. Finally, the minimum and maximum damage-zone sizes observed are also listed.

TABLE 2. SUMMARY OF DAMAGE-ZONE SIZES RESULTING FROM IMPACTS BY 0.4-mm-DIAMETER DROPLETS

Strength Level, MPa	Impact Velocity, m/s	Median Size, μm	Standard Deviation, μm	Min/Max Sizes Observed, μm	No. of Measurements
6.20	96	17	+11 -7	8/65	18
	134	15	+14 -7.5	5/82	67
19.30	64	9	+2 -2	8/10	2
	96	16	+9 -5	8/64	34
	130	12	+9 -6	4/35	29
47.20	96	6	+7 -3	2/20	51
	160	21	+25 -12	14/90	13

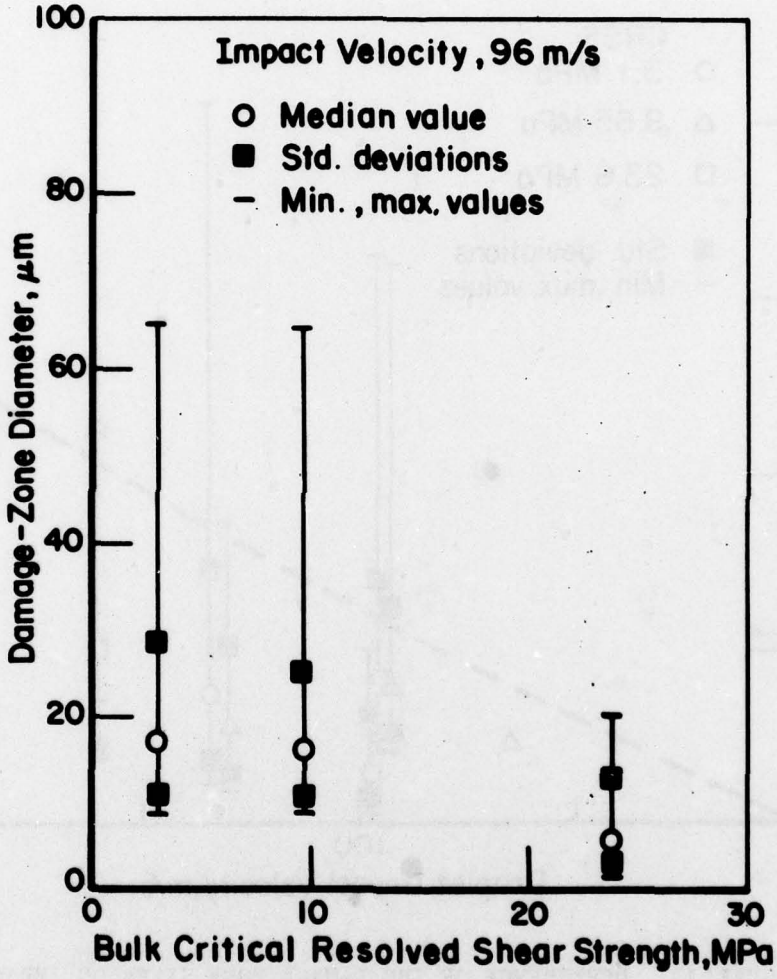

FIGURE 13. RELATION BETWEEN DAMAGE ZONE SIZES AND BULK YIELD STRENGTH FOR IMPACTS AT 96 m/s

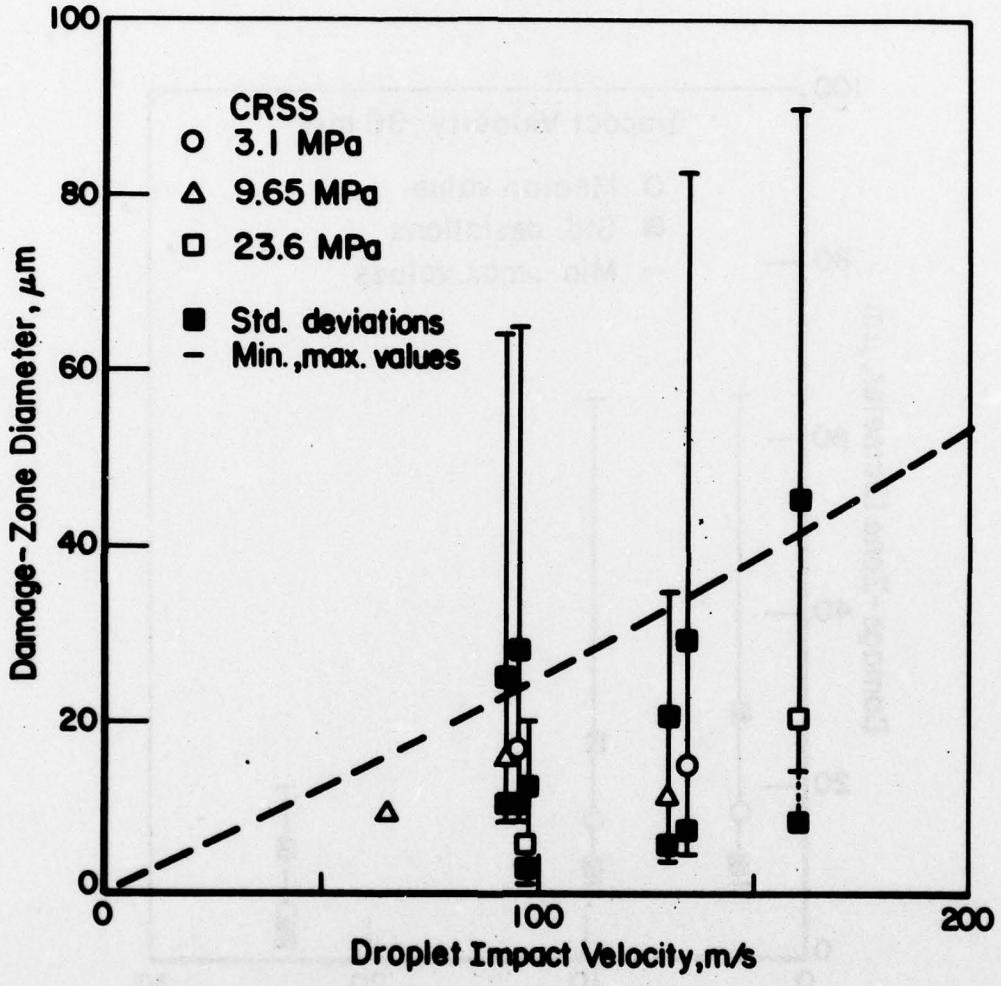

FIGURE 14. DEPENDENCE OF THE DAMAGE ZONE SIZES ON IMPACT VELOCITY FOR THE THREE STRENGTH LEVELS (CRSS, CRITICAL RESOLVED SHEAR STRENGTH) EMPLOYED IN THIS PROGRAM

The dashed line is the predicted critical contact diameter at which the pressure is maximum

Perhaps the most outstanding feature of these results is the magnitude of the spread in damage-zone sizes throughout the range of impact conditions. These spreads likely mask the velocity and bulk yield strength dependence, although some trends are indicated. In Figure 13 a very modest bulk yield strength dependence is observed, although, as described in the preceding section, the results for the unirradiated and 10^6 R materials are nearly identical. The variations in the damage-zone size with impact velocity (Figure 14) are somewhat inconsistent in terms of the median values. For example, at 96 m/s the 10^6 R material displays a median value of 16 μm, but at 130 m/s the median value is only 12 μm. Nevertheless, a trend is apparent showing increasing damage-zone size with impact velocity.

4.7. Multiple Impacts

One specimen from the 10^7 R material was exposed for one minute to a stream of 0.4-mm-diameter droplets impacting at 96 m/s. During this period approximately 18,000 impacts are estimated. Most of the impacts were confined to one side of the specimen, producing the hazy area evident in Figure 15 which is a 13X micrograph of the surface. A thin layer of gold was vapor deposited on the surface to allow scanning electron microscopy. Individual impact sites were also evident in the other half of the specimen. This suggests that the distribution of the impacts may have been Gaussian relative to the centerline of the droplet stream. Within the hazy area, the impact density is estimated to be about $1440/mm^2$, as an average, giving a mean spacing between contact sites of about 40 μm.

The optical micrographs in Figure 16 display several surface features not apparent on the single-impact surfaces. Figure 16a shows the irregular fine relief which dominates the hazy area on the specimen. A number of small craters is also apparent. Some of the craters, such as the example in Figure 16a shows, were associated with a flame-shaped object which in every case extended from the craters in a direction radially away from the axis of the rotation. Figure 16b shows this crater at somewhat higher magnification. Individual impacts could be resolved in the portion of the specimen receiving a low density of impacts. A spectacular example of a crater and surrounding damaged area cuased by one of these impacts is shown in Figure 16c.

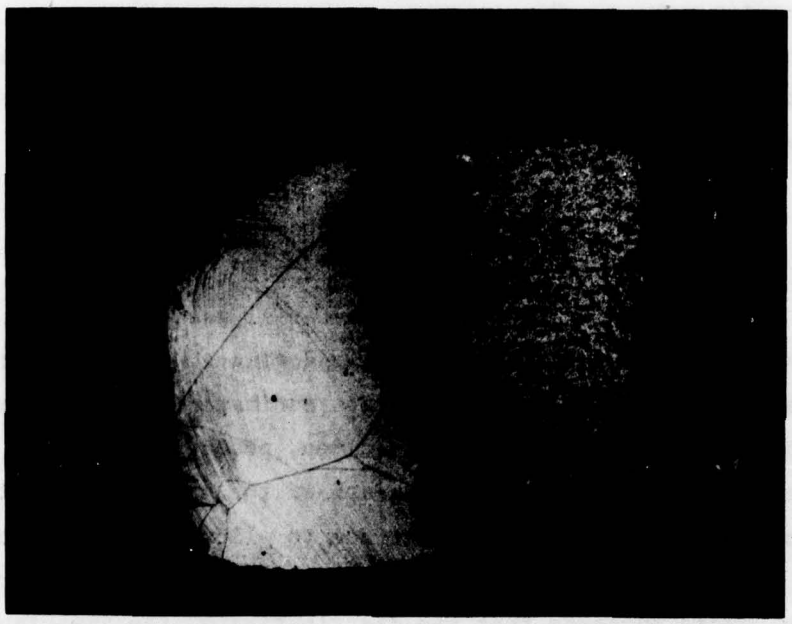

FIGURE 15. A SPECIMEN AFTER EXPOSURE TO APPROXIMATELY 18,000 IMPACTS

The impacts occurred primarily on the right half of the specimen generating the hazy region. The magnification is 12.9X.

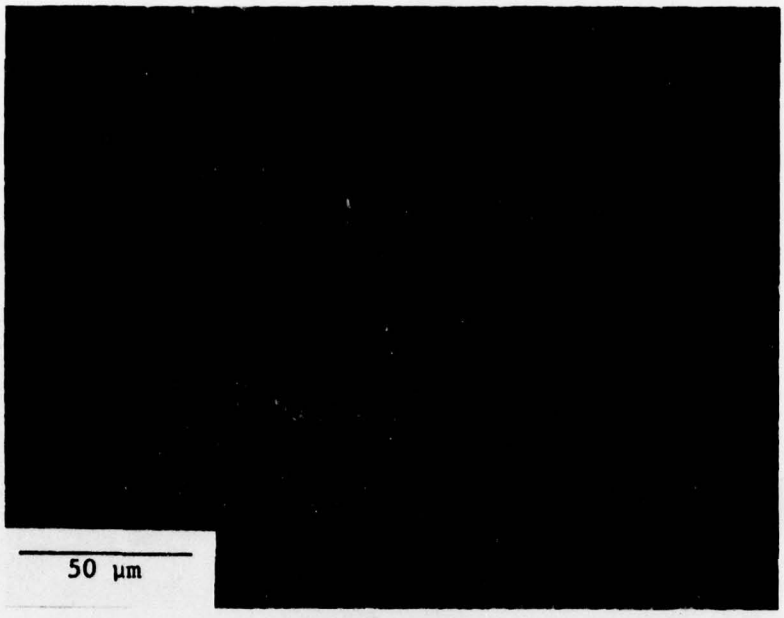

a. A typical area within the heavily impacted region on the specimen. A crater is evident in the center view, attached to an elongated shape which points radially outward from the center of rotation.

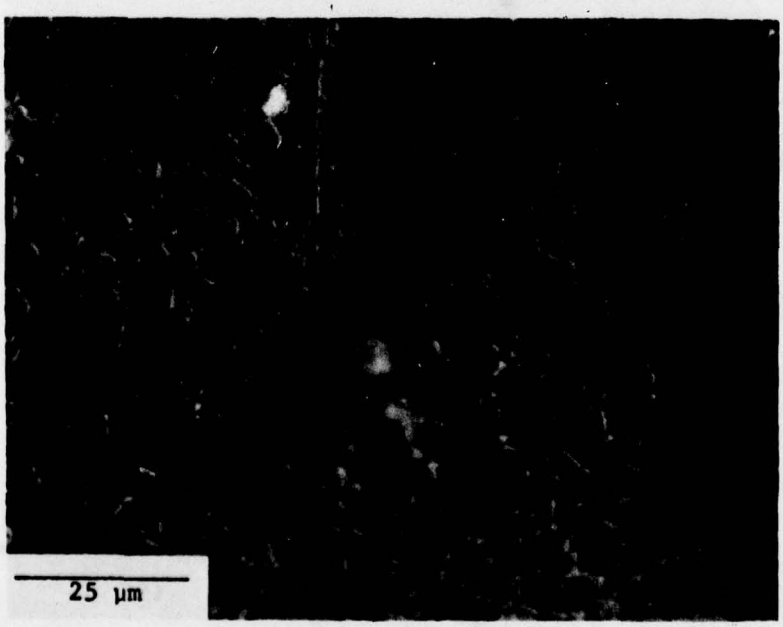

b. A closer view of the crater in (a)

FIGURE 16. EXAMPLES OF SURFACE DAMAGE ON THE MULTIPLY IMPACTED SPECIMEN

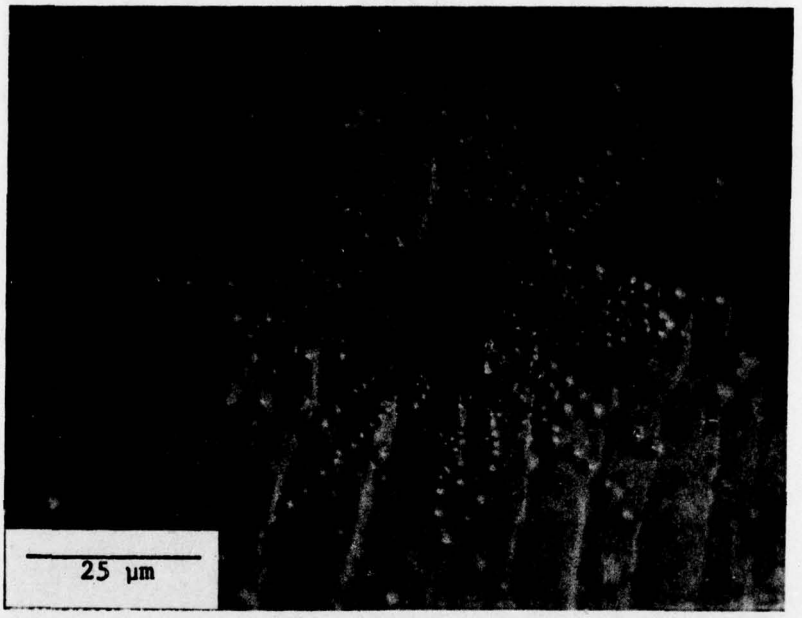

c. A rather spectacular damage zone and crater located in the region of low density impacts

FIGURE 16. (Continued)

Scanning electron microscopy was employed to better identify these features at higher magnification. Figures 17b and 17c are stereo-pairs of elongated objects extending from a crater. Close examination of these objects shows them to be material deposited onto the surface. The appearance of these features suggests that these elongated deposits on the surface had been ejected from the adjoining crater and further that the material was molten at the time of ejection. It is conceivable that the material could be raised to its melting point through adiabatic heating produced by the applied pressure. The pressures required to accomplish this task would be quite large, e.g., on the order of B/10, where B is the bulk modulus. At this time, there are few alternative postulates to explain the occurrence of these features.

4.8. Calculated Pressure Distributions

The numerical simulation of the 100 m/s impact between 0.4 mm diameter water drop and a flat lithium fluoride surface proceded in a fairly satisfactory manner in terms of the calculated pressure distribution over the contact area. A numerical instability developed in the surface and near surface meshes of the lithium fluoride causing oscillating particle velocities which, in turn, precluded an accurate description of the stresses within the lithium fluoride. Unfortunately, these instabilities may have also deteriorated the accuracy of the pressure distribution in the latter portion of the calculation which was terminated after 12 nesc.

Examples of pressure distributions acting upon the contact area at selected times during the impact are contained in Figure 18. The character of the distributions is typical of earlier predictions, i.e. the pressure in the central region of the contact is relatively uniform and increases to a maximum near the edge of the contact area. The magnitude of the central pressure oscillates slightly with time within bounds of about 1 to 2 x 10^8 Pa. This pressure agrees with the simple water-hammer prediction based on the zero-pressure sound speed of 1450 m/s which for a 100 m/s impact is 1.45 x 10^8 Pa. Using the Hugoniot sound speed the water-hammer prediction yields 1.78 x 10^8 Pa. Thus, the pressure in the central region is clearly a simple consequence of the momentum decrease on arresting the axial velocity of the water.

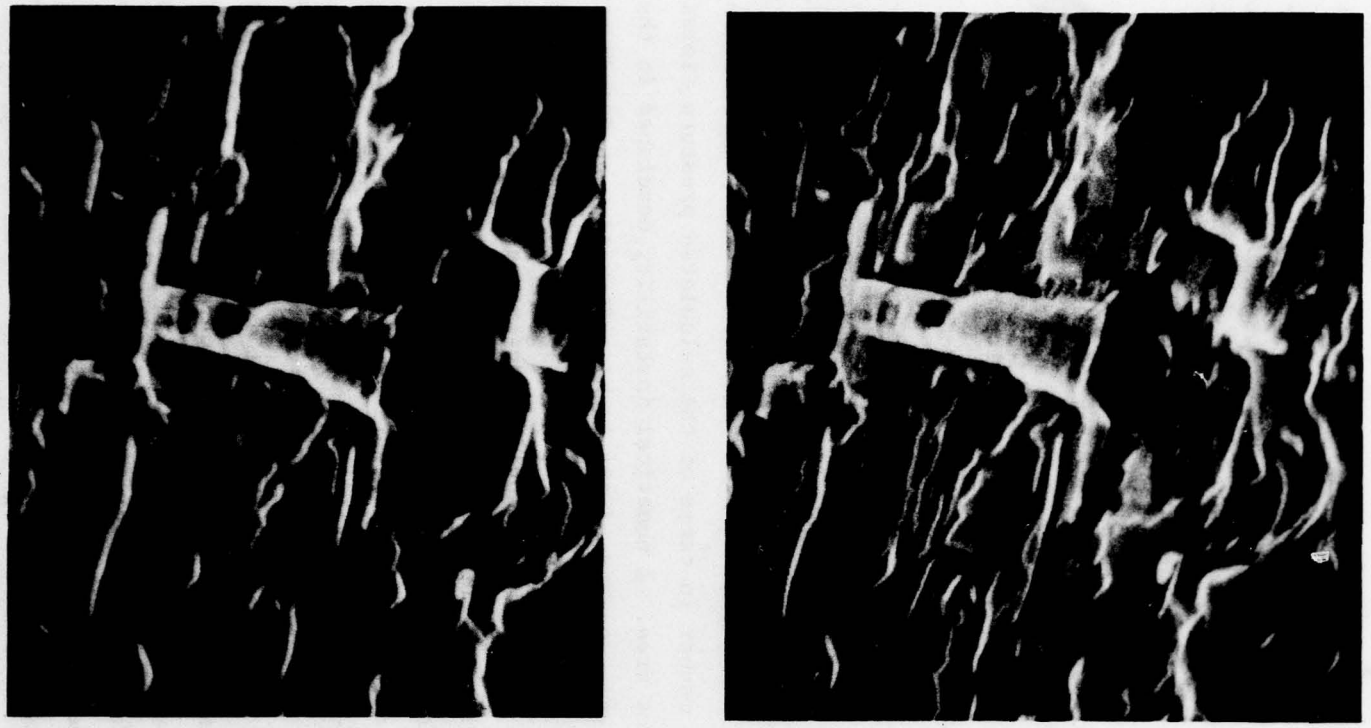

a. Stereopairs showing examples of craters adjacent to elongated structures deposited on the surface

FIGURE 17. SURFACE DAMAGE FEATURES REVEALED BY SCANNING ELECTRON MICROSCOPY

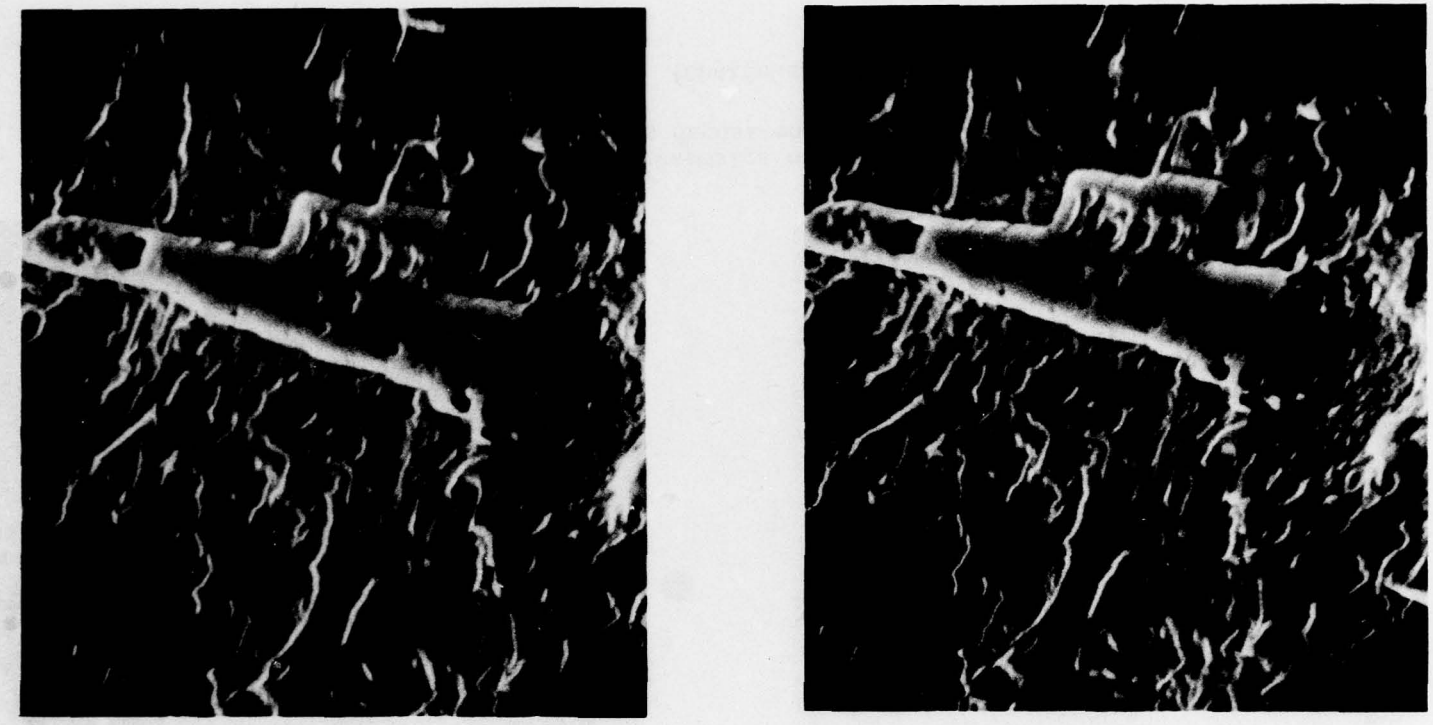

b. Stereopairs showing examples of craters adjacent to elongated structures deposited on the surface

FIGURE 17. (Continued)

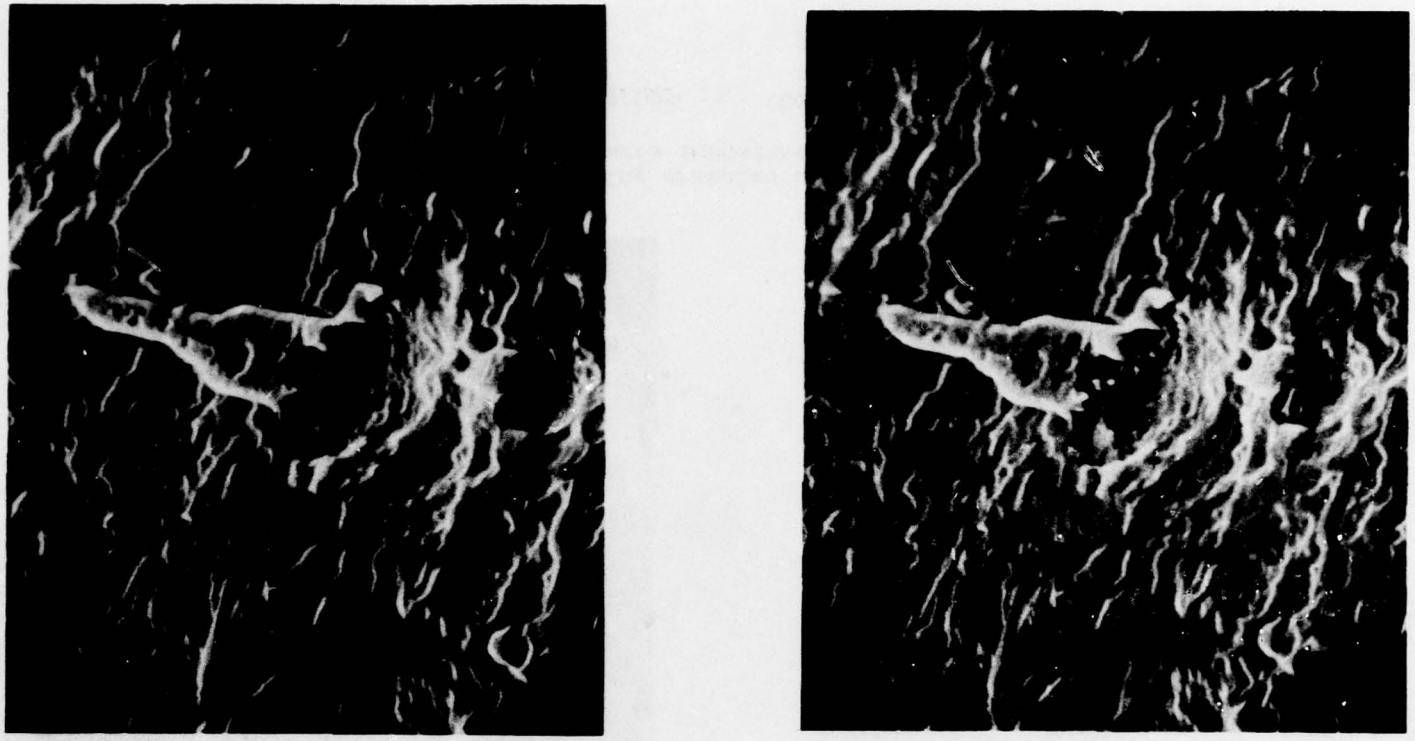

c. Stereopairs showing examples of craters adjacent to elongated structures deposited on the surface

FIGURE 17. (Continued)

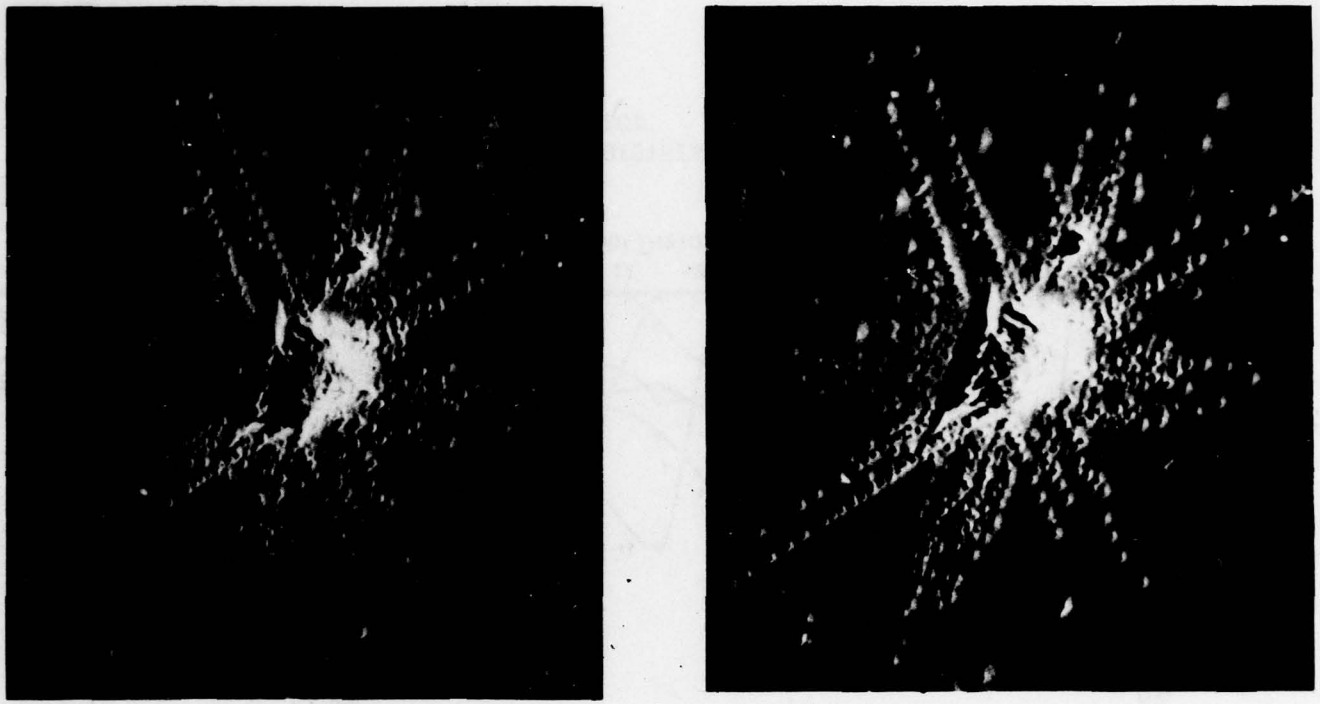

d. A stereopair of the impact site shown optically in Figure 15c

FIGURE 17. (Continued)

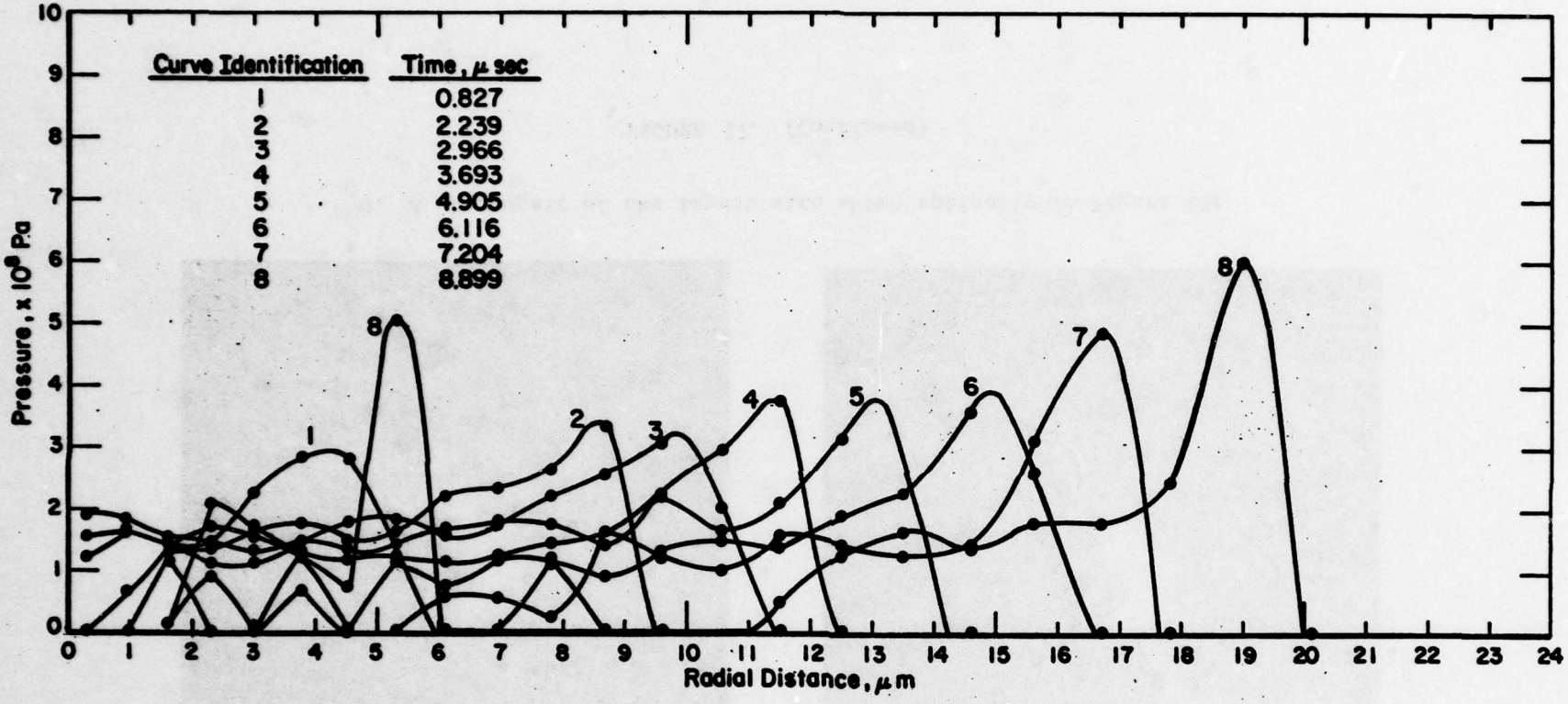

FIGURE 18. CALCULATED PRESSURE DISTRIBUTIONS ON THE CONTACT AREA AT SELECTED TIMES DURING THE IMPACT

Some physical evidence for the evaluation of the pressure near the boundary of the contact area appears when the velocity field within the water drop is examined. An example of a velocity field at a relatively early stage in the impact, about 2.2 nsec. after first contact, is shown in Figure 19. Within an envelope defined by the expanding dilatation wave, significant radial components of the particle velocities exist, and these become larger near the contact periphery. Thus, along this boundary there is fluid flowing in from two directions. At this stage the contact boundary is as effective in arresting the radial velocity as the adjacent solid is in arresting the axial velocities within the drop because the boundary is expanding faster than the sound speed in water. As a consequence the dilatation wave is attached to the boundary. As long as this condition persists the pressure near the boundary will remain above the water hammer level.

The actual peak pressure increases as the contact area expands as shown in Figure 20. There is evidence that the peak pressure is simply the sum of two water hammer pressures, i.e.

$$P_m = P_a + P_r \tag{6}$$

where

$$P_a = \rho CV$$

$$P_r = \rho CU_m$$

and P_m is the peak pressure, P_a the Hugoniot water hammer pressure associated with the axial velocity, V, and P_r is the Hugoniot water hammer pressure associated with the radial velocity, U, at the location of the maximum pressure. Rearranging Equation 6 suggests that the grouping of terms $(P_m - \rho CV)/\rho U_m$ is a constant equal to the sound velocity. The variation of this function with time is shown in Figure 21 in which values of the peak pressures and radial velocities were taken from the calculation at selected times and ρCV was set equal to the Hugoniot value of 1.78×10^8 Pa. After about 3 nsec $(P_m - CV)/U_m$ does become very nearly constant with a value equal to 1500 m/s which is in good agreement with the sound speed. Therefore, Equation 8 is a reasonable description of the peak pressure.

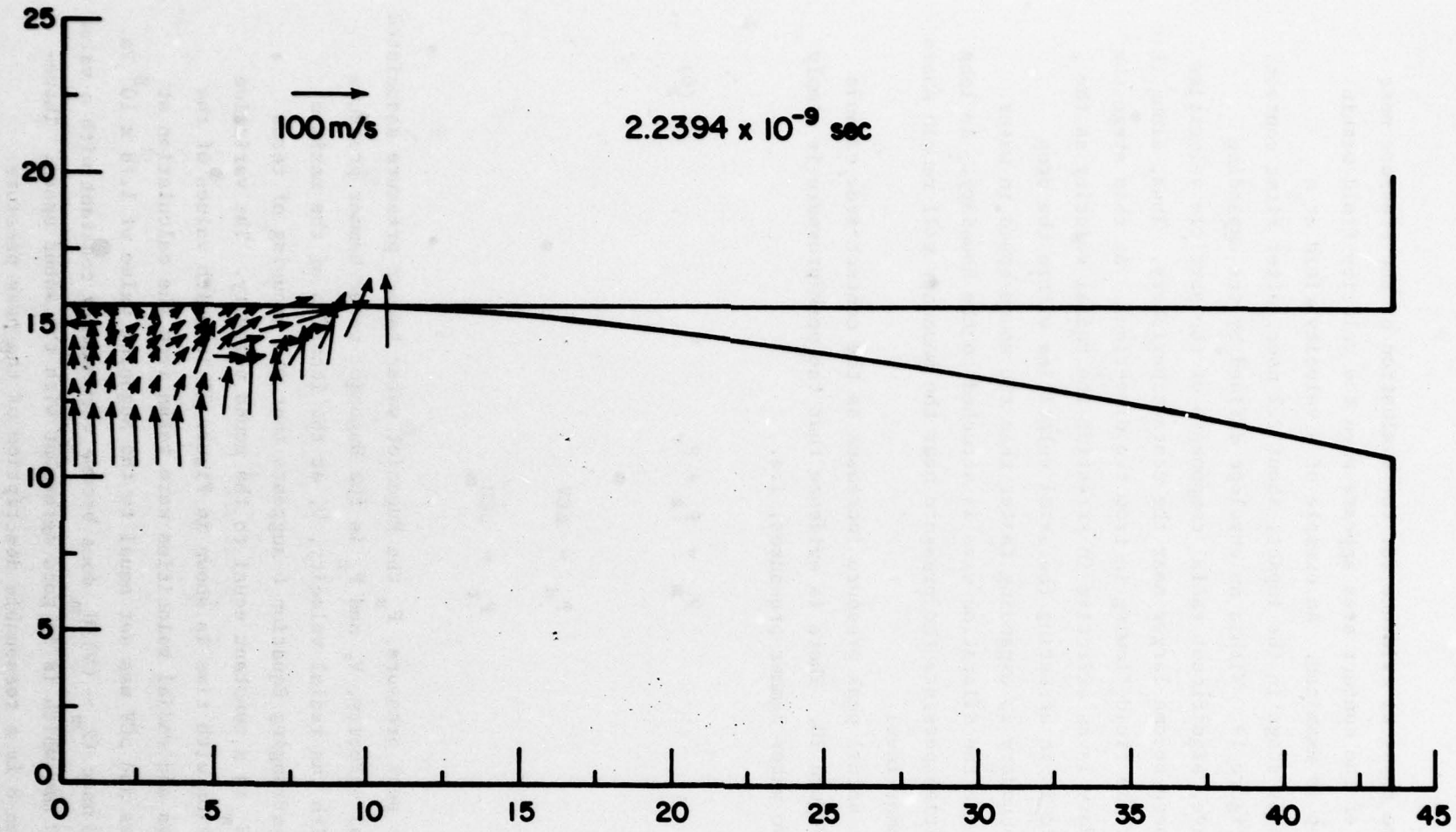

FIGURE 19. THE PARTICLE VELOCITY PATTERN IN THE DROP 2.2394 nsec. AFTER FIRST CONTACT. Only that portion of the velocity field disturbed by the impact is shown.

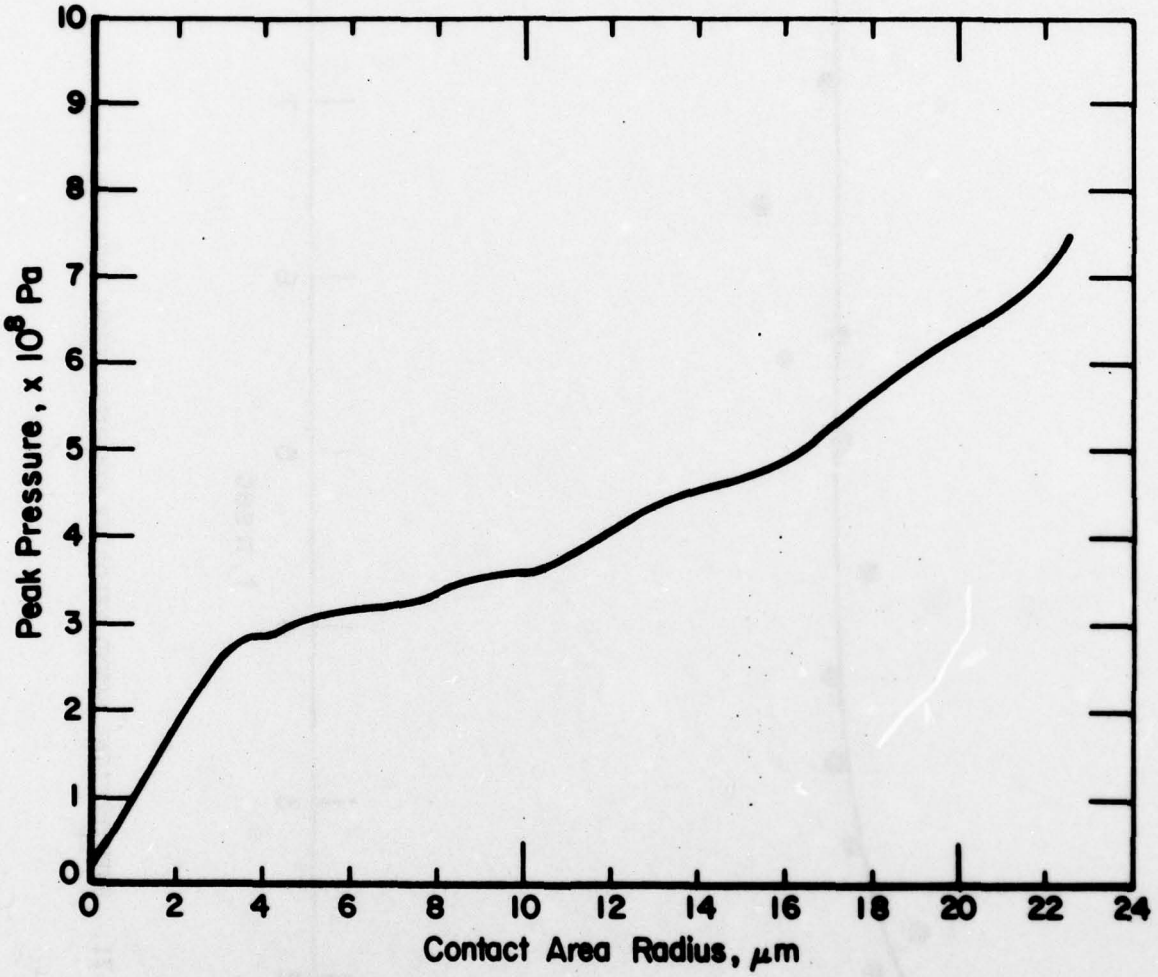

FIGURE 20. CALCULATED DEPENDENCE OF THE PEAK PRESSURE ON THE CONTACT AREA RADIUS

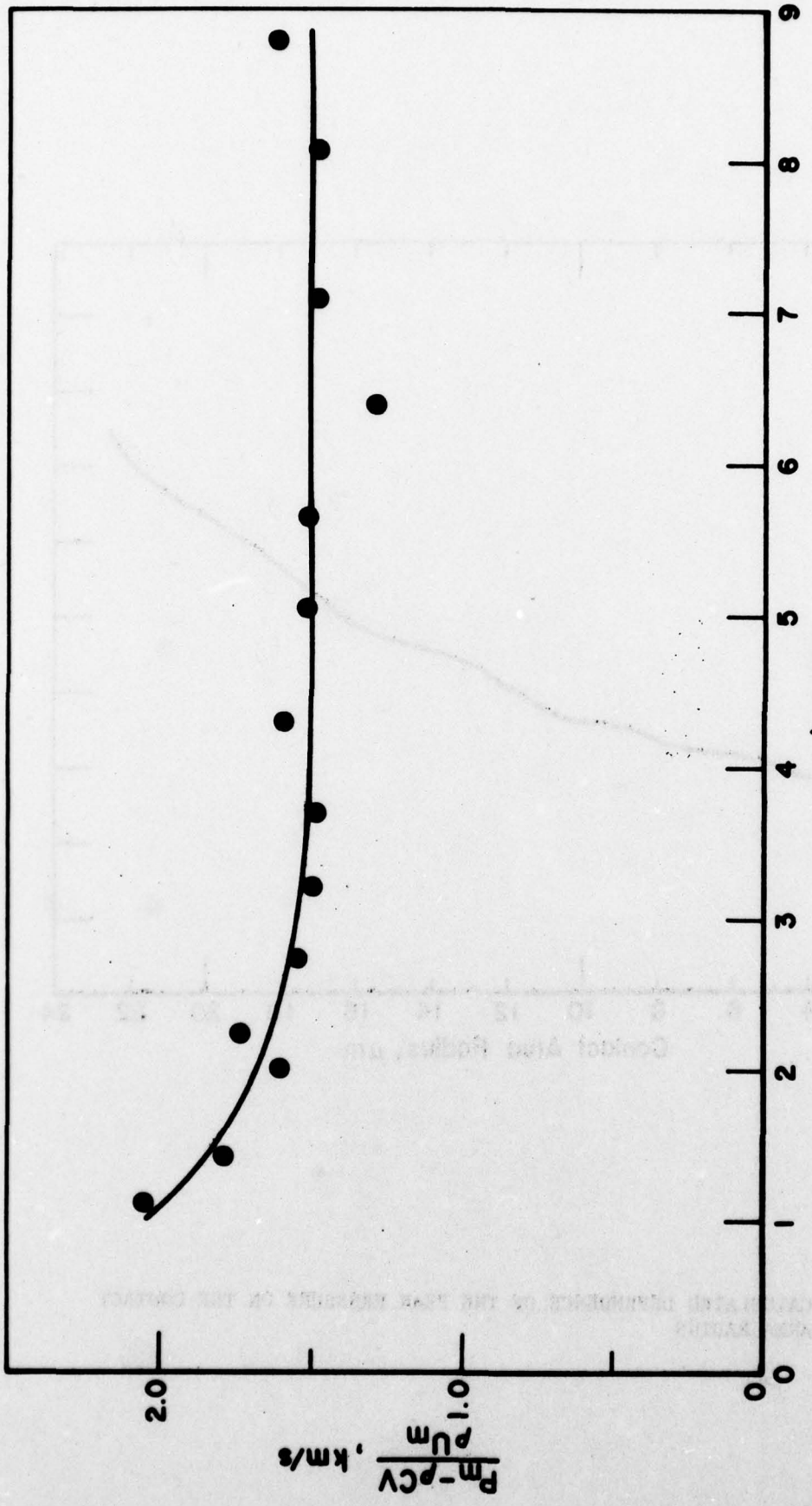

FIGURE 21. HYPOTHETICAL SOUND VELOCITY COMPUTED FROM EQUATION (6).

Initially the spherical drop simply flattens after impact with a relatively rigid surface as shown schematically in Figure 22. Therefore, the contact boundary expands at a rate which decreases with time according to

$$\frac{dr}{dt} = \left(\frac{R}{t} - V\right)\left(\frac{2R}{Vt} - 1\right)^{-1/2} \qquad (7)$$

where H is the drop radius. There is a qualitative argument that the peak pressure should reach its maximum value when the rate of expansion defined by Equation 7 coincides with the sound speed in the fluid. Following this, the wave envelope detaches from the contact boundary allowing the radial expansion of fluid away from the boundary. The critical radius, r_c, i.e. the magnitude of r when dr/dt equals C, is given by

$$r_c = R\left(1 + \frac{C^2}{V^2}\right)^{-1/2}$$

The earlier calculations by Rosenblatt, et al.[7,8] indeed show that the maximum pressure is reached when the radius of the contact boundary is given by Equation 8 and falls precipitously thereafter as the water flows rapidly parallel to the interface. An estimate of the relation between the maximum pressure and impact velocity has been empirically derived from the results of Rosenblatt, et al. and is given as

$$\frac{P_{max}}{P} = 2 + \frac{4V}{C} \qquad (9)$$

where P is the water hammer pressure. It should be noted that this estimate is based on calculations of a 1 mm diameter water drop impacting a rigid surface at 205 m/s and 335 m/s. In our calculations for the case of an impact of a 0.4 mm diameter droplet at 100 m/s the critical contact radius is 13.8 μm at which point the peak pressure is calculated to be about 4.5×10^8 Pa. This is in reasonable agreement with Equation 9 which predicts a maximum pressure of about 4.0×10^8 Pa. Thus, in regard to peak pressure, the two calculations are in agreement. However, in contrast to the Rosenblatt, et al. results, our impact simulation calculation predicts a continued increase in the peak pressure up to the time the calculation was terminated at about 12 nsec. At this time the peak pressure was

7.5×10^8 Pa. The source of this discrepancy is not clear. There is, of course, the possibility that the behavior does not directly scale with drop size and impact speed, and the differences in the pressure-time relations are associated with differences in drop size and impact speed in the two calculations. However, as noted earlier in our calculation, a numerical instability developed in the lithium fluoride which casts a degree of uncertainty on the accuracy of the pressure distributions particularly in the latter portion of the calculation.

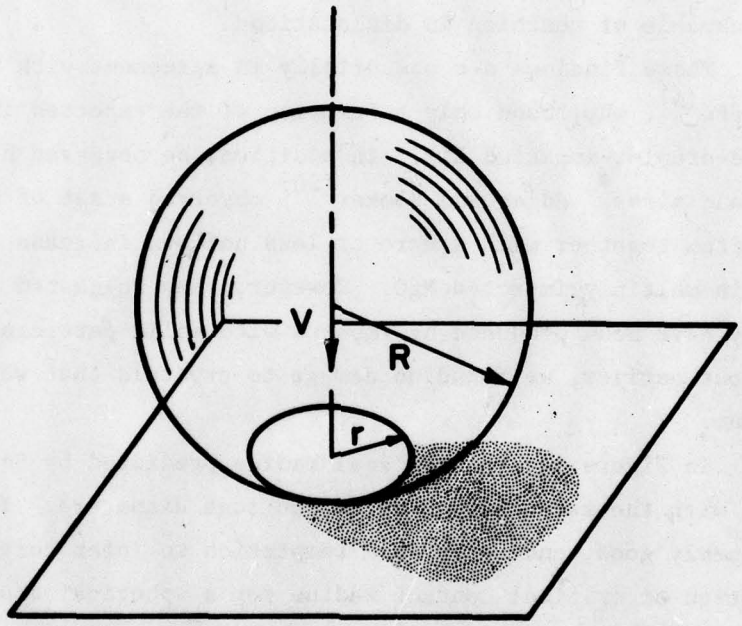

FIGURE 22. SCHEMATIC OF A SPHERICAL DROP IMPACTING A SOLID SURFACE

5. DISCUSSION

The findings in this study lead to an important observation: the stress induced in and/or the plastic response of the LiF during droplet impact are highly variable. Ostensibly identical conditions lead to markedly different consequences. An important implication carried by this observation is that the stresses during impact may range from low levels, sufficient to just move preexisting dislocations, to very high levels, capable of punching in dislocations.

These findings are essentially in agreement with observations of Jolliffe[4], who found only a fraction of the expected impact sites in liquid-droplet-impacted LiF. In addition, he observed highly variable damage-zone sizes. Adler and Hooker[20] observed a set of distinct damage sites together with a more or less uniform increase in dislocation density in multiply impacted MgO. However, they suggested that the damage sites may have been produced by impacts with solid particles of dirt. As pointed out earlier, we found no damage to crystals that were dry run in our system.

In Figure 14, the critical radius predicted by Equation 8 is compared with the measured median damage zone diameters. The comparison is reasonably good, and there is a temptation to infer that the pressure distribution at critical contact radius for a spherical droplet on a flat surface is responsible for the dislocation distributions observed. Indeed, that fact that the critical radius is somewhat larger than the median damage-zone radius can be rationalized in terms of the limiting dislocation velocity. This limiting velocity is the shear wave speed which along the <110> is 3600 m/s in LiF. Appealing to Equation (8) indicates that the contact diameter at which the contact boundary velocity matches this shear wave speed is 10.7 μm for a 96 m/s impact velocity. Clearly, if dislocations were generated prior to this time and were gliding away from the center of contact, they would be unable to keep up with the contact boundary. Furthermore, since the dislocation velocity is stress dependent, there may be insufficient stress to cause the dislocations to "catch up" with the contact boundary before the peak pressure is reached and subsequently falls.

There remains, however, a discrepancy between the stresses required to produce the observed damage and the stresses that can be produced by the calculated pressure distributions. Adler and Hooker[20] calculate a maximum radial stress in the solid which is on the order of one-half the average pressure on the contact area. More importantly, their calculations do not show stresses exceeding the pressure on the contact area. Consistent with these model calculations, we may take, as an upper limit, the maximum normal stress developed in the solid during impact to be about equal to the peak pressure. On this basis, comparing the peak pressures predicted by the numerical results with the yield-strength data in Table 1, it is evident that the stresses produced on impact are more than sufficient to induce bulk plastic flow in all crystals. However, we noted that the damage sites were located in regions devoid of dislocations, i.e., the dislocations comprising the damage were generated during the impact, and further, they were probably punched in from the surface. This process requires stresses on the order of $\mu/10$, which, for LiF, is about 5000 MPa. Similarly in the multiply impacted specimen, evidence of molten material spilling from impact craters was found. An estimate of the pressure required to adiabatically heat the specimen to melting was $B/10$ or about 6500 MPa for LiF. Hence the source of the discrepancy: these stresses are considerably more than an order of magnitude larger than the absolute maximum stress we can expect during impact under the conditions employed in this study.

It is unlikely that further refinements in the model calculations would lead to pressures 20 to 50 times larger. It is equally unlikely that the stresses to punch in dislocations or induce adiabatic melting are 20 to 50 times smaller than the above estimates.

A potential explanation of these discrepancies is that the droplet may not be perfectly spherical or the surface flat as idealized in the model calculations. Indeed, in very general terms, we must appeal to nonuniformities to produce instabilities during the impact in order to generate high peak pressures. One way this might occur has been described by Brunton and Camus[21] who show cavitation within the droplet during impact. The cavitation is produced by the release of pressure after the contact radius exceeds r_c and the droplet begins to undergo high-velocity lateral flow. The subsequent

collapse of these bubbles may be nonuniform, and the internal jet produced on collapse would have a velocity considerably larger than the impact velocity. A collapsing bubble near the surface could generate a very high loading pressure over a small area.

An alternative, albeit hypothetical, source of instability could be the nonuniformities of the droplet surface. If the droplet surface is dented or rippled, one or more large pressure spikes may develop if the contact area happens to include one of these regions of negative curvature. Consider the simple one-dimensional situation of two adjacent contact areas, schematically depicted in Figure 23a. When the contact areas meet, the pressure at the juncture will be elevated over that which existed at the contact boundary just prior to intersection. The amount of elevation depends upon the stage of evolution of the two contact areas. As indicated earlier, the pressure near the contact boundary increases with expansion of the contact area because of radial flow toward the boundary. At intersection, the radial velocities add vectorially, which alters the component of the edge pressure due to radial flow, P_r, identified in Equation (6). Hence, to first order we should expect the pressure increase to be

$$\Delta P \approx P_{r1} + P_{r2} , \qquad (10)$$

where the subscripts 1 and 2 refer to the radial components of pressure associated with Contact Areas 1 and 2, respectively.

Even higher pressures might result from collapse of an entrapped void, such as the annular region idealized in Figure 19b. The collapse of the void could become unstable, producing the jetting action analogous to that which occurs in bubble collapse during cavitation. In addition, if the void has the shape of a spherical cap, its rate of shrinkage will tend to infinity as its diameter approaches zero. This will tend to cause P_r to approach zero. However, lagging behind the rapidly diminishing void boundary will be an annulus of fluid moving as a wave with a group velocity directed radially inward toward the void center. The pressure, P_r, associated with the collapse of this wave should increase approximately as r^{-2}, where r is the radius of the annulus associated with the wave. Thus, shortly after the annihilation of the void, the arrival of the wave with a negative radial particle velocity would tend to increase P_r without limit. It also seems likely that more complex shapes could produce a spectrum of

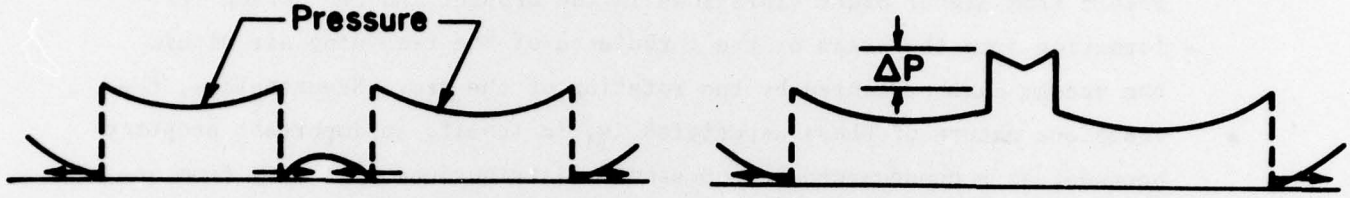

a. The collision of two contact areas produces a local elevation in pressure by ΔP.

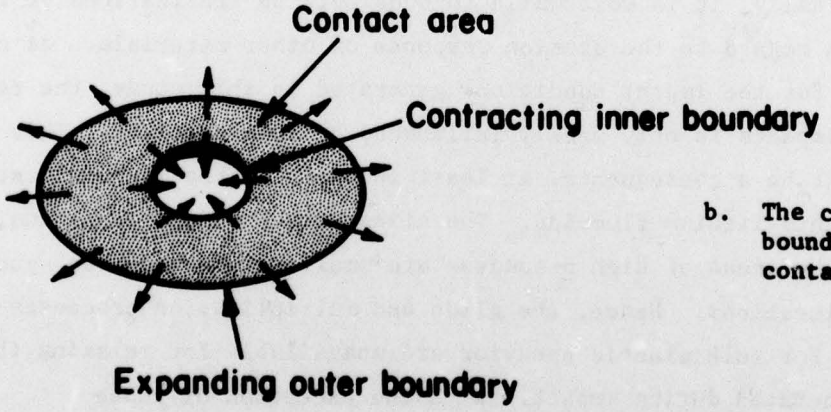

b. The collapse of an internal boundary of an annular contact area.

FIGURE 23. SCHEMATICS OF MULTIPLY CONNECTED CONTACT AREAS DUE TO NONSPHERICAL DROPLET SHAPES

spatial and temporal distributions of pressures, some of which lead to singular pressures.

These descriptions of events that might lead to extraordinary pressures rely on the existence of asperities on the droplet surface. Such asperities, if they exist, would by nature be transient. They may result from higher order vibrations in the droplet induced during its formation from the steam or the turbulence of the remaining air within the vacuum chamber caused by the rotation of the arm. Nevertheless, the transient nature of these asperities is, in itself, an important property because, as a consequence, the pressure distributions will vary from one impact to the next, a feature that clearly agrees with the broad distributions of damage-zone sizes observed.

We have invoked the existence of asperities on the droplet surface in order to provide a possible explanation for our observations of droplet impact damage. It is important that this supposition be checked and examined in more quantitative detail by model calculations. Clearly, calculations need to be performed with nonidealized droplet geometries inserted into the initial conditions.

Finally, it is worthwhile to consider the implications of these results with regard to the erosion response of other materials. As noted previously, for the impact conditions generated in this study, the response to droplet impacts is only weakly influenced by bulk strength. This behavior must be a consequence, at least in part, of the low dislocation density in this lithium fluoride. The sizes of the damage zones and, therefore, the areas of high pressures are smaller than the mean spacing between dislocations. Hence, the glide and multiplication processes responsible for bulk plastic behavior are unavailable for relaxing the stresses generated during impact. With the exception of those examples where preexisting dislocations had moved, the lithium fluoride responds as an essentially elastic solid during the impact until the high-pressure spike occurs. We might expect, therefore, that materials with much higher initial dislocation densities would respond plastically during the entire impact. This raises the possibility that the course of the impact would be altered by plastic flow in the solid, e.g., plastic indentation early in the impact event which would affect the subsequent lateral jetting. The important point, however, is that <u>if</u> the preexisting

dislocation structure contributes to the relaxation of the stresses generated by impact, the damage response will be more sensitively dependent upon bulk flow properties. This becomes an important consideration in terms of possible benefits to erosion resistance to be gained by manipulation of bulk mechanical properties.

6. CONCLUSIONS

1. The consequences of an individual droplet impact cannot be predicted with certainty for impacts to 160 m/s. In the case of impact on single-crystal LiF with a low initial dislocation density, the damage is defined by a probability distribution. At about 100 m/s, for example, the impact damage by 0.4-mm-diameter droplets ranges from movement of preexisting dislocations to generation of dislocation rosettes 60 to 80 μm in size.
2. The bulk yield strength of the LiF exerts a very weak influence on the median of the damage size distribution. Similarly, in the range of 60 to 160 m/s the median is relatively insensitive to the impact velocity.
3. To explore the prospect that peak pressures derived from numerical calculations are inversely related to mesh sizes and time increments in models of droplet impact events, a calculation was conducted using a much more finely divided model than earlier calculations. Although a portion of the results of this calculation remain open to question, the predicted peak pressures when the contact area has grown to its critical diameter are only slightly higher than earlier predictions. These pressures are incapable of producing the damage observed in the experiments.
4. Observations of dislocations generated in initially dislocation-free areas and observations of apparently molten and resolidified material point to the existence of very high pressures during impact. The implication is that the pressures are 20 to 50 times higher than predictions by hydrodynamic calculations of spherical droplet impact. A theoretical argument for the generation of pressure singularities is advanced. The argument relies on the existence of transient asperities in the droplet surface, a feature that is plausible but remains to be established.

7. REFERENCES

(1) Gould, G. C., "Some Observations on Erosion by Cavitation and Impingement", in Characterization and Determination of Erosion Resistance, ASTM STP 474, Phila., (1970), p. 182.

(2) Heymann, F. J., "On the Time Dependence of the Rate of Erosion Due to Impingement or Cavitation", in Erosion by Cavitation or Impingement, ASTM STP 408, Phila., (1961), p. 70.

(3) Hackworth, F. J., Kocher, L. H., and Snell, I. C., "The Response of Infrared Transmitting Materials to High Velocity Impact by Water Drops", presented at ASTM Symposium on Erosion Prevention and Useful Applications, Vail, Colorado, October 1977.

(4) Jolliffe, K. H., "The Application of Dislocation Etching Techniques to the Study of Liquid Impacts", Phil. Trans. Roy. Soc., 260, (1960), p. 101.

(5) Huang, Y. C., Hammitt, F. G., and Yang, W. J., "Hydrodynamic Phenomena During High-Speed Collision Between Liquid Droplet and Rigid Plane", J. Fluid Eng., Trans. ASME, 95, (1973), p. 276.

(6) Hwang, J. G., and Hammitt, F. G., "High-Speed Impact Between Curved Liquid Surface and Rigid Flat Surface", J. Fluid Eng., Trans. ASME, 99, (1977), p. 396.

(7) Rosenblatt, M., Eggum, G. E., DeAngelo, L. A., and Kreyenbagen, K. N., "Numerical Investigation of Water Drop Erosion Mechanisms in Infrared-Transparent Materials", AFML-TR-76-193, December, 1976.

(8) Ito, Y. M., Rosenblatt, M., Perry, F. W., and Eggum, G. E., "Analysis of Water-Drop Erosion Mechanisms in Infrared-Transparent Materials Using Microphysical Fracture Models", AFML-TR-77-219, October, 1977.

(9) Heymann, F. J., "High-Speed Impact Between Liquid Drop and a Solid Surface", J. Appl. Phys., 40, (1969), p. 5113.

(10) Nadeau, J. S., "Color Centers and the Flow Stress of LiF Single Crystals", J. Appl. Phys., 33, (1962), p. 3480.

(11) Hoagland, R. G., Marschall, C. W., Rosenfield, A. R., Holleberg, G., and Ruh, R., "Microstructural Factors Influencing Fracture Toughness of Hafnium Titanate", Mater. Sci. Eng., 15, (1974), p. 51.

(12) Gilman, J. J., "Direct Measurements of the Surface Energies of Crystals", J. Appl. Phys., 31, (1960), p. 2208.

(13) Gilman, J. J., Knudsen, C., and Walsh, W. P., "Cleavage Cracks and Dislocations in LiF Crystals", J. Appl. Phys., 29 (1958), p. 601.

(14) Lindblad, N. R., and Schneider, J. M., "Production of Uniform-Sized Liquid Droplets", J. Sci. Instr., 42, (1965), p. 635.

(15) Hageman, L. J. and Walsh, J. M., "HELP, A Multi-Material Eulerian Program for Compressible Fluids and Elastic-Plastic Flows in Two Space Dimensions and Time", Vol. I, Rpt. 3SR-350, Systems Science and Software, La Jolla, California, May, 1971.

(16) Gurtman, G. A., Kirsch, J. W., and Hastings, C. R., "Analytical Equation of State for Water Compressed to 300 kbar", J. Appl. Phys., 42, (1971).

(17) Bridgman, P. W., "Linear Compressions to 30000 kg/cm^2, Including Relatively Incompressible Substances", Proc. Am. Acad. Arts and Sciences, 77, (1949), p. 187.

(18) Hirth, J. P., "The Influence of Surface Structure on Dislocation Nucleation", Proceedings of Conference on the Relation Between the Structure and Mechanical Properties of Metals, Her Majesty's Stationary Office, London, England (January, 1963), p. 217.

(19) Nabarro, F.R.N., Theory of Crystal Dislocation, Clarendon Press, Oxford, England (1967), p. 75.

(20) Adler, W. F., and Hooker, S. V., "Impact Damage in Single Crystals", Technical Report to Office of Naval Research, TR77-49, July 1977.

(21) Brunton, J. H., and Camus, J. J., "The Flow of a Liquid Drop During Impact", Proceedings of the Third International Conference on Rain Erosion and Associated Phenomena, Royal Aircraft Establishment, United Kingdom, 1970, p. 327.

(22) Landolt-Bornstein Tables, K. H. Hellwege and A. M. Hellwege (Eds.), Springer-Verlag, Berlin, West Germany (1966), Vol. I.

BASIC DISTRIBUTION LIST

Technical and Summary Reports

Organization	No. of Copies
Defense Documentation Center Cameron Station Alexandria, Virginia 22314	(12)
Office of Naval Research Department of the Navy	
Attn: Code 471	(1)
Code 102	(1)
Code 470	(1)
Commanding Officer Office of Naval Research Branch Office 495 Summer Street Boston, Massachusetts 02210	(1)
Commanding Officer Office of Naval Research Branch Office 536 South Clark Street Chicago, Illinois 60605	(1)
Office of Naval Research San Francisco Area Office 760 Market Street, Room 447 San Francisco, California 94102	
Attn: Dr. P. A. Miller	(1)
Naval Research Laboratory Washington, D.C. 20390	
Attn: Code 6000	(1)
Code 6100	(1)
Code 6300	(1)
Code 6400	(1)
Code 2627	(1)
Naval Air Development Center Code 302 Warminster, Pennsylvania 18974	
Attn: Mr. F. S. Williams	(1)
Naval Air Propulsion Test Center Trenton, New Jersey 08628	
Attn: Library	(1)
Naval Construction Batallion Civil Engineering Laboratory Port Hueneme, California 93043	
Attn: Materials Division	(1)
Naval Electronics Laboratory Center San Diego, California 92152	
Attn: Electron Materials Sciences Division	(1)
Naval Missile Center Materials Consultant Code 3312-1 Point Mugu, California 93041	(1)
Commanding Officer Naval Surface Weapons Center White Oak Laboratory Silver Spring, Maryland 20910	
Attn: Library	(1)
David W. Taylor Naval Ship R&D Center Materials Department Annapolis, Maryland 21402	(1)
Naval Undersea Center San Diego, California 92132	
Attn: Library	(1)
Naval Underwater System Center Newport, Rhode Island 02840	
Attn: Library	(1)
Naval Weapons Center China Lake, California 93555	
Attn: Library	(1)
Naval Postgraduate School Monterey, California 93940	
Attn: Mechanical Engineering Dept.	(1)
Naval Air Systems Command Washington, D.C. 20360	
Attn: Code 52031	(1)
Code 52032	(1)
Code 320	(1)

BASIC DISTRIBUTION LIST (Cont'd)

Organization	No. of Copies
Naval Sea System Command Washington, D.C. 20362 Attn: Code 035	(1)
Naval Facilities Engineering Command Alexandria, Virginia 22331 Attn: Code 03	(1)
Scientific Advisor Commandant of the Marine Corps Washington, D.C. 20380 Attn: Code AX	(1)
Naval Ship Engineering Center Department of the Navy CTR BG #2 3700 East-West Highway Prince Georges Plaza Hyattsville, Maryland 20782 Attn: Engineering Materials and Services Office, Code 6101	(1)
Army Research Office Box CM, Duke Station Durham, North Carolina 27706 Attn: Metallurgy & Ceramics Div.	(1)
Army Materials and Mechanics Research Center Watertown, Massachusetts 02172 Attn: Res. Programs Office (AMXMR-P)	(1)
Air Force Office of Scientific Research Bldg. 410 Bolling Air Force Base Washington, D.C. 20332 Attn: Chemical Science Directorate Electronics and Solid State Sciences Directorate	(1) (1)
Air Force Materials Lab (LA) Wright-Patterson AFB Dayton, Ohio 45433	(1)

Organization	No. of Copies
NASA Headquarters Washington, D.C. 20546 Attn: Code RRM	(1)
NASA Lewis Research Center 21000 Brookpark Road Cleveland, Ohio 44135 Attn: Library	(1)
National Bureau of Standards Washington, D.C. 20234 Attn: Metallurgy Division Inorganic Materials Division	(1) (1)
Defense Metals and Ceramics Information Center Battelle Memorial Institute 505 King Avenue Columbus, Ohio 43201	(1)
Director Ordnance Research Laboratory P.O. Box 30 State College, Pennsylvania 16801	(1)
Director Applied Physics Laboratory University of Washington 1013 Northeast Fortieth Street Seattle, Washington 98105	(1)
Metals and Ceramics Division Oak Ridge National Laboratory P.O. Box X Oak Ridge, Tennessee 37380	(1)
Los Alamos Scientific Laboratory P.O. Box 1663 Los Alamos, New Mexico 87544 Attn: Report Librarian	(1)
Argonne National Laboratory Metallurgy Division P.O. Box 229 Lemont, Illinois 60439	(1)

BASIC DISTRIBUTION LIST (Cont'd)

Organization	No. of Copies	Organization	No. of Copies
Brookhaven National Laboratory Technical Information Division Upton, Long Island New York 11973 Attn: Research Library	(1)		
Library Building 50 Room 134 Lawrence Radiation Laboratory Berkeley, California	(1)		

SUPPLEMENTARY DISTRIBUTION LIST

Dr. W. F. Adler
Effects Technology Inc.
5383 Hollister Avenue
P.O. Box 30400
Santa Barbara, CA 92105

Dr. G. Bansal
Battelle
505 King Avenue
Columbus, OH 43201

Dr. R. Bratton
Westinghouse Research Lab.
Pittsburgh, PA 15235

Mr. T. Derkus
TRW
Cleveland, OH 44117

Dr. A. G. Evans
Rockwell International
P.O. Box 1085
1049 Camino Dos Rios
Thousand Oaks, CA 91360

Mr. E. Fisher
Ford Motor Co.
Dearborn, MI

Dr. P. Gielisse
University of Rhode Island
Kingston, RI 02881

Dr. M. E. Gulden
International Harvester Company
Solar Division
2200 Pacific Highway
San Diego, CA 92138

Dr. S. Hart
Naval Research Laboratory
Washington, D.C. 20375

Dr. D. P. H. Hasselman
Montana Energy and MHD Research
and Development Institute
P.O. Box 3809
Butte, Montana 59701

Mr. G. Hayes
Naval Weapons Center
China Lake, CA 93555

Professor A. H. Heuer
Case Western Reserve University
University Circle
Cleveland, OH 44106

Dr. R. Hoagland
Battelle
505 King Avenue
Columbus, OH 43201

Dr. R. Jaffee
Electric Power Research Institute
Palo Alto, CA

Dr. P. Jorgensen
Stanford Research Institute
Poulter Laboratory
Menlo Park, CA 94025

Dr. R. N. Katz
Army Materials and Mechanics
Research Center
Watertown, MA 02171

Professor G. Kino
Stanford University
Palo Alto, CA 94305

Dr. H. Kirchner
Ceramic Finishing Company
P.O. Box 498
State College, PA 16801

SUPPLEMENTARY DISTRIBUTION LIST (Cont'd)

Dr. B. Koepke
Honeywell, Inc.
Corporate Research Center
500 Washington Avenue, South
Hopkins, MN 55343

Mr. Frank Koubek
Naval Surface Weapons Center
White Oak Laboratory
Silver Spring, MD 20910

E. Krafft
Carborundum Co.
Niagara Falls, NY

Dr. J. Krumhansl
Physics Department
Cornell University
Ithica, NY 14850

Dr. F. F. Lange
Rockwell International
P.O. Box 1085
1049 Camino Dos Rios
Thousand Oaks, CA 91360

Dr. J. Lankford
Southwest Research Institute
8500 Culebra Road
San Antonio, TX 78284

Library
Norton Company
Industrial Ceramics Division
Worcester, MA 01606

State University of New York
College of Ceramics at Alfred University
ATTN: Library
Alfred, NY 14802

Dr. R. E. Loehman
University of Florida
Ceramics Division
Gainesville, FL 32601

Dr. N. MacMillan
Materials Research Laboratory
Pennsylvania State University
College Park, PA 16802

Mr. F. Markarian
Naval Weapons Center
China Lake, CA 93555

Dr. F. A. McClintock
Massachusetts Institute of Technology
Department of Mechanical Engineering
Cambridge, MA 02139

Dr. Perry A. Miles
Raytheon Company
Research Division
28 Seyon Street
Waltham, MA 02154

Dr. D. Mulville
Office of Naval Research
Code 474
800 North Quincy Street
Arlington, VA 22217

Dr. N. Perrone
Office of Naval Research
Code 474
800 North Quincy Street
Arlington, VA 22217

Dr. J. R. Rice
Brown University
Division of Engineering
Providence, RI 02912

Mr. R. Rice
Naval Research Laboratory
Code 6360
Washington, D.C. 20375

Dr. J. Ritter
University of Massachusetts
Department of Mechanical Engineering
Amherst, MA 01002

Professor R. Roy
Pennsylvania State University
Materials Research Laboratory
University Park, PA 16802

Dr. R. Ruh
AFML
Wright-Patterson AFB
Dayton, Ohio 45433

Mr. J. Schuldies
AiResearch
Phoenix, AZ

Professor G. Sines
University of California, Los Angeles
Los Angeles, CA 90024

Dr. N. Tallan
AFML
Wright-Patterson AFB
Dayton, Ohio 45433

Dr. R. A. Tanzilli
General Electric Company
Reentry and Environmental Systems Division
3198 Chestnut Street
Philadelphia, PA 19101

Dr. T. Vasilos
AVCO Corporation
Research and Advanced Development
Division
201 Lowell Street
Wilmington, MA 01887

Mr. J. D. Walton
Engineering Experiment Station
Georgia Institute of Technology
Atlanta, GA 30332

Dr. S. M. Widerhorn
Inorganic Materials Division
National Bureau of Standards
Washington, DC 20234

Dr. N. Corney
Ministry of Defence
The Adelphi
John Adam Street
London WC2N 6BB
UNITED KINGDOM

Professor John Field
University of Cambridge
New Cavendish Laboratory
Cambridge,
UNITED KINGDOM

Dr. L. M. Gillin
Aeronautical Research Laboratory
P.O. Box 4331
Fisherman's Bend
Melbourne, VIC 3001
AUSTRALIA

Dr. B. R. Lawn
Physics Department
University New South Wales
Kingston, New South Wales
AUSTRALIA